


REPORT DOCUMENTATION PAGE				Form Approved OMB No. 0704-0188	
The public reporting burden for this collection of information is estimated to average 1 hour per response, including the time for reviewing instructions, searching existing data sources, gathering and maintaining the data needed, and completing and reviewing the collection of information. Send comments regarding this burden estimate or any other aspect of this collection of information, including suggestions for reducing the burden, to the Department of Defense, Executive Services and Communications Directorate (0704-0188). Respondents should be aware that notwithstanding any other provision of law, no person shall be subject to any penalty for failing to comply with a collection of information if it does not display a currently valid OMB control number.					
PLEASE DO NOT RETURN YOUR FORM TO THE ABOVE ORGANIZATION.					
1. REPORT DATE (DD-MM-YYYY) 06-04-2007		2. REPORT TYPE Final		3. DATES COVERED (From - To) 1 Feb 2004 - 30 Dec 2006	
4. TITLE AND SUBTITLE Fluidic Control of Virtual Aerosurfaces				5a. CONTRACT NUMBER	
				5b. GRANT NUMBER FA9550-04-1-0028	
				5c. PROGRAM ELEMENT NUMBER	
				5d. PROJECT NUMBER	
6. AUTHOR(S) Dr. Ari Glezer				5e. TASK NUMBER	
				5f. WORK UNIT NUMBER	
7. PERFORMING ORGANIZATION NAME(S) AND ADDRESS(ES) Woodruff School of Mechanical Engineering Georgia Institute of Technology Atlanta, GA 30332-0405				8. PERFORMING ORGANIZATION REPORT NUMBER	
9. SPONSORING/MONITORING AGENCY NAME(S) AND ADDRESS(ES) Air Force Office of Scientific Research 875 N. Randolph Street, Suite 325, Room 3112 Arlington, VA 22203-1768				10. SPONSOR/MONITOR'S ACRONYM(S) AFRL/AFOSR	
				11. SPONSOR/MONITOR'S REPORT NUMBER(S)	
12. DISTRIBUTION/AVAILABILITY STATEMENT Distribution A: Approved for public release; distribution unlimited.				AFRL-SR-AR-TR-07-0423	
13. SUPPLEMENTARY NOTES					
14. ABSTRACT This experimental research has focused on modifying the global aerodynamic characteristics of lifting surfaces at cruise (low) angles of attack when the baseline flow is fully attached. Using hybrid actuators, trapped vorticity concentrations at the leading and trailing edges affect aerodynamic forces and moment without control surfaces. Hybrid actuators employ miniature [O(0.01c)] obstructions with integrated synthetic jet actuators. Actuation on the pressure surface near the leading edge ($x/c=0.21$) results in a substantial (up to 50%) reduction in pressure drag and total drag (29%) with virtually no loss in lift, leading to a higher lift to drag ratio. When the actuation is applied near the trailing edge, the effects are bi-directional changes in pitching moments (up to ± 0.65 CMO), which can be continuously varied by controlling the actuation amplitude. Moreover, the same performance can be achieved at substantially reduced actuation power by exploiting transitory aerodynamic effects through pulse modulation. PIV studies of the flow in the vicinity of the actuators, in the boundary layer and the wake, were used in this investigation.					
15. SUBJECT TERMS flow control; synthetic jet; hybrid actuators; PIV; drag reduction; lift-to-drag ratio; cruise aerodynamics					
16. SECURITY CLASSIFICATION OF:			17. LIMITATION OF ABSTRACT		18. NUMBER OF PAGES
a. REPORT U	b. ABSTRACT U	c. THIS PAGE U	UU		71
19a. NAME OF RESPONSIBLE PERSON					19b. TELEPHONE NUMBER (Include area code)

FLUIDIC CONTROL OF VIRTUAL AEROSURFACES

AFOSR Grant FA9550-04-1-0028

FINAL REPORT

submitted by

Ari Glezer

Woodruff School of Mechanical Engineering

Georgia Institute of Technology

ABSTRACT

The present research program has focused on modifications of the global aerodynamic characteristics of lifting surfaces at cruise (low) angles of attack when the baseline flow is fully attached. Aerodynamic forces and moments are effected by trapped vorticity concentrations without moving control surfaces the generation and accumulation (trapping) of vorticity near the leading and trailing edges of the lifting surfaces is managed by integrated hybrid actuators comprised of miniature $[O(0.01c)]$ small obstructions and synthetic jet actuators. The present work has demonstrated that the presence of controllable trapped vorticity concentrations can result in several complimentary aerodynamic effects. Actuation on the pressure surface near the leading edge ($x/c = 0.21$) results in a substantial (up to 50%) reduction in pressure drag and a reduction of 29% in total drag with virtually no loss in lift and therefore higher lift to drag ratio. When the actuation is applied near the trailing edge, the primary effects are bi-directional changes in the pitching moments (up to $\pm 0.65C_{M0}$) without moving control surfaces. These changes can be continuously varied by controlling the actuation amplitude. Moreover, by exploiting transitory aerodynamic effects through pulse modulated actuation near the trailing edge, it is possible to maintain the same aerodynamic performance at substantially reduced actuation power. Particle image velocimetry (PIV) studies of the flow in the vicinity of the actuators and in the wake and boundary layer of the airfoil were used to investigate the creation and manipulation of trapped vorticity near the hybrid actuator and the resulting effects on the airfoil aerodynamic characteristics.

20071024051

I. INTRODUCTION

Strategies for active flow control on lifting surfaces employing fluidic actuation have primarily focused on mitigation of partial or complete flow separation in order to improve aerodynamic performance. Prior studies have demonstrated significant aerodynamic effects that occur as a result of application of steady suction and blowing (e.g. Chang 1976 and Attinello 1961) or pulsed blowing (e.g. Seifert et al. 1996). However, substantial quantities of mass flux are required to achieve any significant effect using these methods; this difficulty is overcome through the use of synthetic jets, which were used by Smith and Glezer (2002) to manipulate a much larger steady jet.

Active flow control techniques can be divided into two categories according to the (reduced) frequency at which they operate. In many instances, the primary focus has been on mitigation of partial or complete flow separation over stalled wing sections or flaps where the separating shear layer is dominated by a strong coupling to the instability of the wake that leads to the nominally time-periodic formation and shedding of large-scale vortices (e.g., Wu et al. 1998). Therefore, attempts to manipulate and ultimately control separation in aerodynamic systems have relied on the narrow-band receptivity of the separating, wake-dominated flow to external actuation at a Strouhal number that corresponds to the unstable frequency of the wake. As noted by Glezer et al. (2005) the actuation induces a Coanda-like deflection of the shed vortices towards the surface of the stalled airfoil and consequently to lift enhancement.

A different approach to flow control that is *decoupled* from the global flow (wake) instabilities was developed at Georgia Tech and emphasizes fluidic modification of the “apparent” aerodynamic shape of the surface by exploiting the interaction between arrays of surface-mounted synthetic jet actuators and the local cross flow (Glezer and Amitay 2002). The interaction domain between the jet and the cross flow is in effect a trapped vorticity concentration where the actuator jet regulates a balance between the trapped and shed vorticity concentrations that are coupled with local changes in the streamwise pressure gradient. The work at Georgia Tech has demonstrated that the formation of these interaction domains upstream of flow separation can result in complete or partial bypass (or suppression) of separation (e.g., Amitay et al. 1998, 2001 and Amitay and Glezer 2002). Control is attained at actuation frequencies that are at least an order of magnitude higher than the characteristic flow frequency

$[St_{act} \sim O(10)]$ and therefore decoupled from global flow instabilities. It is noted that the use of trapped vorticity to alter the apparent local surface curvature and the direction of the flow over lifting surfaces is not new and was explored in a number of earlier investigations as early as the 1950s using stationary, mechanically trapped vortices (e.g., Perkins and Hazen 1953 and Hurley 1959).

Because this approach to flow control is decoupled from the global instability of the base flow, it can be effective not only when the baseline flow is separated but also when it is fully attached, namely at cruise conditions at low angles of attack. Chatlynne et al. (2001) and Amitay et al. (2001) showed that the formation of a stationary trapped vortex above an airfoil at low angles of attack leads to a reduction in pressure drag that is comparable to the magnitude of the pressure drag of the baseline configuration with minimal lift penalty. Actuation was accomplished using a hybrid actuator comprised of a synthetic jet downstream from a miniature surface-mounted passive obstruction of scale $O(0.01c)$ and the extent and strength of the trapped vortex was varied by varying the actuation frequency. In the present studies, hybrid actuators each consisting of a small passive obstruction of size $O(0.01c)$ similar to a Gurney flap combined with an integral synthetic jet actuator are used on the surface of an airfoil to create and manipulate concentrations of trapped vorticity in order to improve aerodynamic performance.

A Gurney flap is a flat plate that is typically mounted along the trailing edge of a conventional airfoil and normal to its lower (pressure) surface such that its height is on the order of the boundary layer thickness. As noted by Liebeck (1978) (and confirmed by wind tunnel testing of a flap of height $0.0125c$ on a symmetric Newman airfoil), a flap having a characteristic height smaller than $0.02c$ can lead to simultaneous increase in lift and reduction in drag. Although Liebeck (1978) noted that the mechanism for drag reduction was not well understood, he nevertheless suggested a possible mechanism as illustrated in Figure I.1. It was conjectured that the drag reduction results from the displacement of small adjacent separation bubbles (essentially a counter-rotating vortex pair) that form along the upper and lower surfaces of the airfoil just upstream of its trailing edge (Figure I.1a). These bubbles extend into the near wake and a stagnation point is formed along the dividing streamline that extends to the trailing edge. The downwash associated with the increased lift in the presence of the Gurney flap apparently results in displacement and stretching of the separation bubbles (Figure I.1b) and therefore in a smaller velocity deficit within the wake of the airfoil.

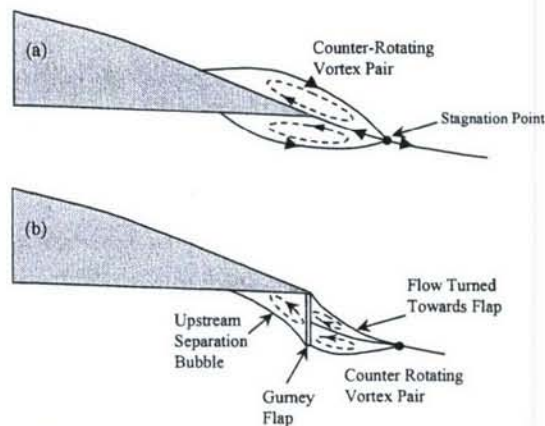


Figure 1.1. Conjectured flow structure near the trailing edge of an airfoil with a Gurney flap. (From Liebeck 1978).

The formation of the counter rotating vortex pair downstream of a Gurney flap was later demonstrated computationally on a cambered airfoil profile by Jang (1992). Jeffrey et al. (2000) confirmed this experimentally, showing how a Gurney flap increases circulation over the airfoil by inducing the equivalent of a stationary vortex located near the trailing edge. Some evidence in the literature (e.g., Myose et al. 1998) suggests that drag reduction by Gurney flaps is more readily achieved on symmetric rather than on cambered airfoils. Also, other types of trailing edge flaps similar to a Gurney flap, including wedge-shaped and angled flaps, have been used to affect aerodynamic performance in a manner comparable to a Gurney flap (e.g. Bloy et al. 1997 and Richter et al. 2002). Of particular note from the standpoint of the effects of trapped vorticity is the work of Carrannanto et al (1998) who used a passive Gurney flap like tab to modify the venting flow upstream of a deployed trailing edge flap to engender concentrations of trapped vorticity and thereby significantly improve the aerodynamic performance of the flap and maintain fully attached flow on the flap.

As noted above, the objective of the present work is to vary the aerodynamic performance of an airfoil by manipulating the trapped vortices that are induced near the surface of the airfoil by a miniature hybrid actuator that is essentially similar to an *active* Gurney flap. The trapped vorticity downstream of the actuator's passive obstruction is controlled by an integrated synthetic jet actuator. Actuators are placed at several key locations along the airfoil including the pressure side near the leading edge and the pressure and suction sides near the trailing edge with

significant *complimentary* effects on the global aerodynamic forces and moments at low angles of attack when the flow over the airfoil is fully attached.

II. EXPERIMENTAL APPARATUS AND TECHNIQUES

II.1 Airfoil Model

The experiments described in this report are conducted using a swept airfoil model with a uniform cross section with a sweep angle of 27.1° . The chord length in the streamwise direction is 501 mm and the span is approximately 1.0 m, corresponding to the width of the wind tunnel in which it is installed. The cross section is based on a commercial aircraft configuration and contains an inflection point on the pressure surface near the trailing edge, as shown in Figure II.1. The model is made of fiberglass and features a smooth finished surface lacking seams or protrusions. Metal end plates are used to attach the model to a pair of coaxial pegs by which it is mounted in a wind tunnel using frictional couplings; this arrangement permits the airfoil to be securely restrained in the tunnel while allowing the angle of attack to be set arbitrarily in a range spanning $-5^\circ < \alpha < 10^\circ$. Springloaded pins on the endplates with attached rubber pads press against the side walls of the wind tunnel, further securing the model in place; the pins are located as far as practical from the mounting pegs to ensure that the model remains at a constant angle of attack.



Figure II.1. Airfoil model with actuator.

A cavity in the interior of the model permits a wide variety of flow control hardware to be installed on the airfoil. Access is provided by a removable rhombus-shaped panel at midspan measuring approximately one third of the span to which flow control hardware is attached (see below). The panel is flush mounted to the surface of the airfoil, and all gaps and fasteners are sealed to minimize disturbances to the flow. Multiple panels, identical except for the particular flow control hardware attached, are used to test the model under various configurations; a panel without flow control hardware is used to obtain baseline measurements.

The model is installed in an open return wind tunnel with a test section having a square cross section of nominal size 1.0 m. Flow through the inlet is generated by a primary fan driven by a

130 kW motor that is connected to a speed controller. Downstream of the fan, the flow passes through a diffuser containing straightening vanes and screens into a plenum, which is connected to the test section by a converging section having an area ratio of 9:1. This system produces a flow in the test section that is nominally at atmospheric pressure, with a maximum speed of 42 m/s and a turbulence level of 0.2%. Movable panels located on two opposing walls of the test section can be adjusted so that the pressure is uniform in the streamwise direction, thus diminishing the effects of the wind tunnel walls on the flow around the model.

The entire airfoil (including the removable panels) is instrumented with a circumferential array of 70 pressure ports located at mid-span. Additional pressure ports located on the synthetic jet modules can be included as necessary. Each port is connected to a Pressure Systems, Inc. Model 98RK NetScanner digital pressure measurement system consisting of five 16-port modules with a range of 2.5 kPa. The system produces simultaneous measurements of the static pressure at multiple locations on the airfoil with an accuracy of 4 Pa. Data from the scanner is transferred to a PC running the National Instruments, Inc. LabView software package, which is used for storage and analysis of the pressure measurements.

II.2 Hybrid Actuators

Control of the flow is accomplished using various configurations of hybrid actuators installed on the airfoil. Each hybrid actuator consists of a small obstruction having a characteristic cross stream dimension of $O[0.01c]$ integrated with a synthetic jet actuator. Within the actuator is a central cavity containing piezoelectric discs and a small rectangular orifice in the plane of the airfoil sweep line through which the jet exits. In the present investigations, two different types of hybrid actuators are used.

One of the hybrid actuators used is surface-mounted and contains four piezoelectric discs of diameter 31.75 mm. The actuator is in the shape of a wedge of length 159 mm and height 8.3 mm, or $0.017c$ in terms of the airfoil chord, and contains a rounded surface on the downstream end which is designed to exploit the Coanda effect. Located at the upstream end of the rounded surface is a small backward facing step of height 1.5 mm which contains the actuator orifice. Owing to the orientation of the orifice, which is rectangular and has dimensions of 150 mm in length and 0.4 mm in height, the jet is directed in the downstream direction. The center of the orifice is located 1.0 mm from the corner of the wedge, as illustrated in Figure II.2. The actuator

and rounded surface are also equipped with ports for static pressure measurement, one of which is located at the actuator orifice. The actuator is operated at a frequency of $f_{\text{act}} = 1770$ Hz, corresponding to a resonance of the actuator cavity. At a freestream speed of $U_{\infty} = 30$ m/s, the reduced frequency of the actuator is $St_{\text{act}} = 29.5$, and the maximum momentum coefficient is $C_{\mu} = 0.9 \cdot 10^{-4}$. The Stokes number has a value of 10.9.

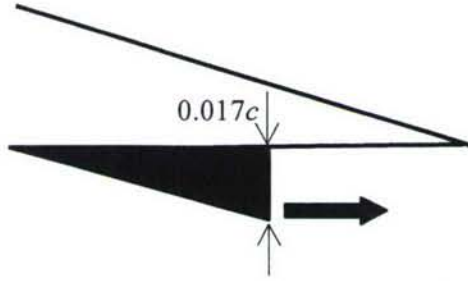


Figure II.2. Detail of actuator configuration; the jet produced by the actuator is denoted by the large arrow.

A second type of hybrid actuator used in these studies is designed to be embedded in the removable airfoil cover (see above). This actuator is of rectangular shape with dimension of 300 mm x 36 mm x 8.9 mm and contains sixteen piezoelectric discs, eight of which are on either side of a central cavity. A curved slot connects the cavity to a rectangular orifice located near one of the long edges of the actuator body that is oriented to produce a jet in the downstream direction. Like the wedge-type actuator, this hybrid actuator is also fitted with a rounded Coanda surface downstream of the orifice containing static pressure ports. The upstream facing surface can be equipped with one of several fairings with different slopes, each of which contain static pressure ports. The actuator operates at a cavity resonance frequency of $f_{\text{act}} = 2250$ Hz, corresponding to a reduced frequency of $St_{\text{act}} = 38$ at a freestream speed of 30 m/s. At this speed the maximum momentum coefficient is $C_{\mu} = 0.9 \cdot 10^{-4}$, and the Stokes number is 12.3.

II.3 Particle Image Velocimetry (PIV)

Phase-locked and time averaged PIV are used on and near the airfoil centerline to characterize the flowfields near the hybrid actuator and in the wake, as well as in the boundary layer around the entire airfoil. PIV analyses are predominantly conducted in the cross-stream plane $z = 0$; however, as noted in §III.2.2, some measurements are taken in a plane normal to the airfoil sweepline.

A digital PIV system is used to obtain pairs of images of the flowfield for crosscorrelation. The flow is seeded with particles of theatrical fog fluid of size $O[1 \mu\text{m}]$ using a slotted airfoil located in the wind tunnel plenum along the centerline (see above). A double pulse Nd-YAG laser illuminates the particles in the flow; this is accomplished by passing the circular beam through a system of cylindrical and spherical lenses and the transparent walls of the wind tunnel to produce a narrow laser sheet of approximate thickness 1 mm. Normal to the plane of the laser sheet is a 1000×1016 pixel CCD camera capable of acquiring pairs of images separated by a brief time interval at a maximum rate of 15 Hz. Images from the camera (at spatial resolutions ranging from 13 to $142 \mu\text{m} / \text{pixel}$) are digitized and stored for further analysis using a PC with a frame grabber board. A synchronizer controlled by the PC operates the camera and lasers at appropriate times to produce pairs of images of particles in the flowfield which can be processed using the crosscorrelation routine in a commercial PIV software package.

Vector fields from the crosscorrelation software are used to calculate quantities such as mean velocity, Reynolds stresses, and vorticity. In turn, these data are used to determine additional characteristics of the flow including the vorticity flux and circulation around the airfoil as well as the properties of the airfoil boundary layer. A software package developed in-house is used to join multiple vector fields in different locations into a single high-resolution vector field, permitting analysis of large regions of the flow.

III. TRAPPED VORTICITY NEAR THE TRAILING EDGE

This section of the report describes the aerodynamic effects of vorticity concentrations near the trailing edge and the effective modification of the Kutta condition. In this configuration, the pressure surface of the airfoil ($c = 501$ mm) is equipped with a hybrid actuator of characteristic height $0.017c$, the orifice of which is located at $x/c = 0.93$. The actuator operates at a reduced frequency of $St_{act} = 110$ and contains an orifice of width 0.4 mm. The present measurements in this configuration are conducted at $Re_c = 3.3 \cdot 10^5$. The earlier work of DeSalvo et al. (2002) showed that the aerodynamic effects of an inactive hybrid Gurney flap are similar to the effects of a conventional Gurney flap located at the trailing edge of the same airfoil. The measured aerodynamic forces were comparable to the forces effected by conventional Gurney flaps on cambered airfoils (e.g., Jeffrey et al. 2000 and Giguère et al. 1995), as well as the CFD results of Jang (1992).

III.1 Continuous Actuation

The effect of jet actuation on the pressure distribution around the airfoil when the hybrid actuator is placed at $x/c = 0.93$ is shown in Figures III.1a and b for $\alpha = 4^\circ$ and 8° , respectively. It is noted that because the flow does not stagnate at the leading edge due to the sweep of the airfoil, the maximum pressure coefficient observed near the leading edge is on the order of 0.8 . Compared to the baseline configuration, the addition of the Gurney flap leads to a decrease in pressure on the suction surface of the airfoil and a corresponding increase on the pressure surface particularly for $x/c > 0.65$ (similar effects on the pressure distribution for a conventional Gurney flap were observed by Giguère et al. 1995). It is noteworthy that the presence of the actuator on the pressure side leads to an increase in pressure upstream of the actuator ($x/c = 0.93$) and a corresponding decrease in pressure downstream of the actuator owing to the suction induced by the local separation domain. One immediate consequence of these pressure changes is an increase in lift; however, there is also an increase in drag because of the lower pressure on the downstream section of the suction surface. Compared to the smooth airfoil, the increase in lift that results from the decrease in pressure on the suction surface appears to be accompanied by increased downward turning of the flow above the airfoil and a reduction in the pressure near the trailing edge. However, as noted in connection with Figure III.2b, the increase in lift is also accompanied by an increase in pressure drag.

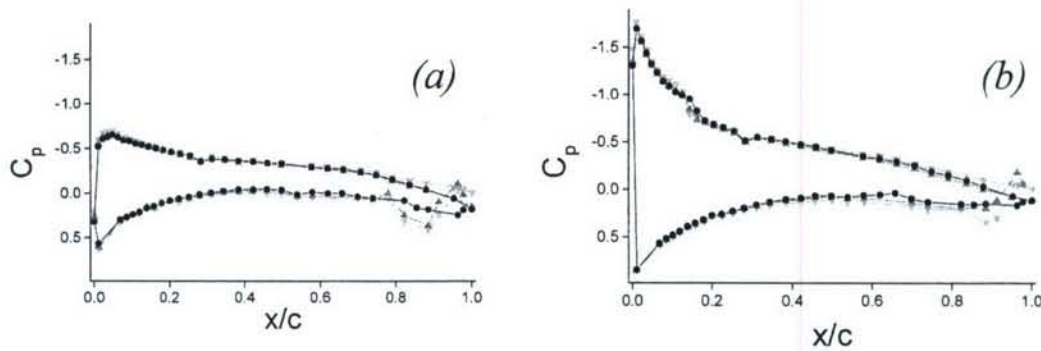


Figure III.1. Pressure distribution around the airfoil for (a) $\alpha = 4^\circ$ and (b) $\alpha = 8^\circ$. (●) Baseline, (▼) actuator not operating, (▲) continuous actuation.

Actuation ($C_\mu = 8 \cdot 10^{-3}$) results in an increase in the pressure distribution on the suction side of the airfoil and a slight decrease in pressure upstream of the actuator on the pressure side. It is remarkable that the pressure distribution along the entire upper (suction) surface of the airfoil when the jet is operating is higher than in the absence of actuation and is virtually identical to the pressure distribution of the smooth airfoil. At the same time, while the pressure along the pressure side of the airfoil is generally lower than when the jet is inactive, it is still higher than for the smooth airfoil and the blockage effect that is induced upstream of the hybrid Gurney flap on the pressure side is somewhat diminished (this change is more pronounced at $\alpha = 8^\circ$, Figure III.1b). The actuation also results in an expansion of the lower (suction) pressure domain between the downstream edge of the actuator and the trailing edge of the airfoil. This is shown by the presence of a suction peak at $x/c = 0.96$ where the pressure coefficient is lower than in the absence of actuation.

As shown in Figures III.5a-b below, the actuation causes the flow to turn upward (toward the trailing edge), accounting for the increase in the trailing edge pressure. The upward tilt is commensurate with the slight reduction in lift that is caused by the increased pressure on the suction surface and the suction peak on the lower surface ($x/c = 0.93$). The upward turning of the flow near the jet orifice is similar to the turning (vectoring) of a primary jet toward a low-pressure interaction domain that is induced by an adjacent synthetic jet actuator, which was investigated in detail by Smith and Glezer (1998).

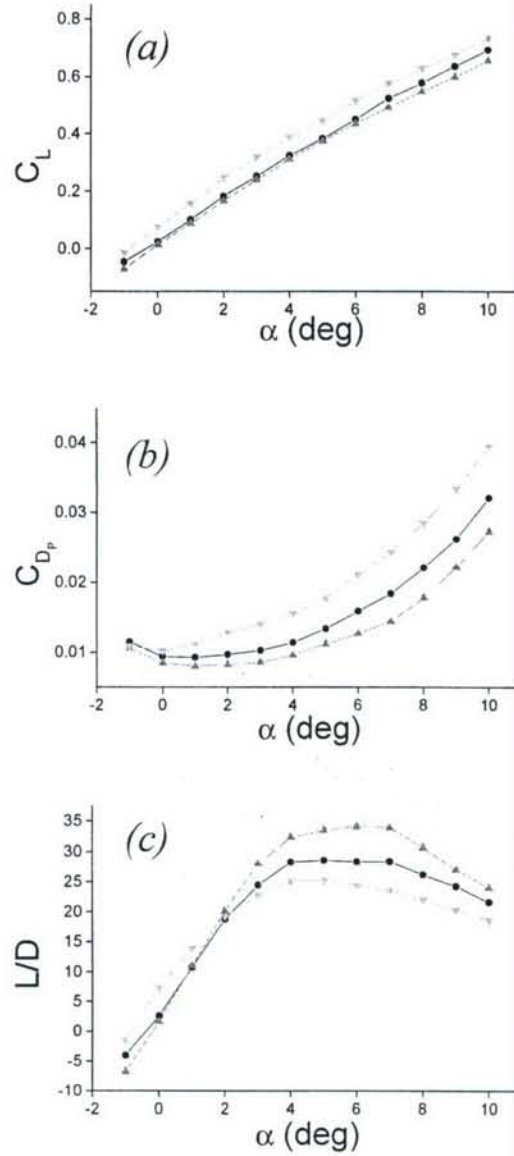


Figure III.2. Variation with angle of attack of (a) C_L , (b) C_{Dp} , and (c) L/D_p . (●) Baseline, (▼) actuator not operating, (▲) continuous actuation.

The effect of the actuation on the aerodynamic characteristics of the airfoil for angles of attack within the range $-1^\circ < \alpha < 10^\circ$ is shown in Figure III.2. Although the addition of the hybrid actuator at $x/c = 0.93$ results (in the absence of actuation) in an increase in lift (Figure III.2a), a simultaneous increase in pressure drag (Figure III.2b) leads to an overall decrease in L/D_p compared to the baseline (smooth) airfoil (Figure III.2c). When actuation is applied ($C_\mu = 8 \cdot 10^{-3}$), the lift decreases (the decrement $\Delta C_L \approx 0.07$ is almost independent of angle of attack), and is

very close to the lift coefficient of the smooth airfoil even though the hybrid Gurney actuator is present. These data show that for a given C_L , the actuation leads to a decrease in the pressure drag compared to the effect of an unactuated flap and even to the smooth (baseline) airfoil. Therefore, the reduction in drag when the actuation is applied leads to a substantial increase in L/D_p over the entire range of angles of attack (Figure III.2c). At this streamwise position of the hybrid actuator, the maximum lift to pressure drag ratio is obtained at $\alpha = 6^\circ$ ($L/D_p = 34.1$), which is an increase of 40% over L/D_p of the unactuated flap, but more significantly an increase of more than 20% relative to the smooth airfoil.

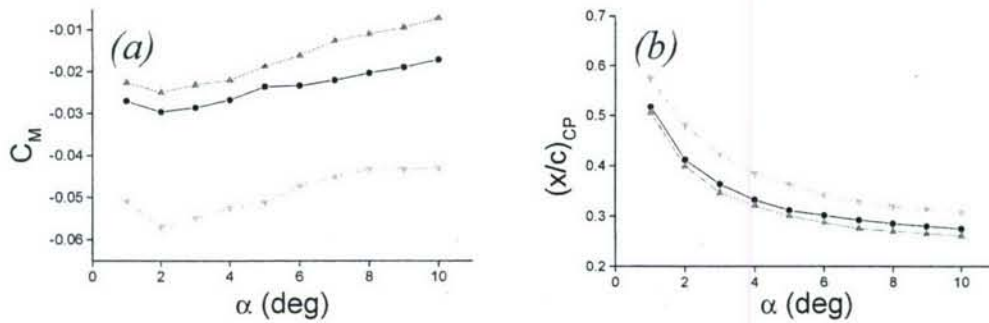


Figure III.3. Variation of (a) moment coefficient about $c/4$ and (b) center of pressure location. (●) Baseline, (▼) actuator not operating, (▲) continuous actuation.

The effects of forcing on the moment coefficient (about $c/4$) and streamwise center of pressure location are shown in Figure III.3 for $1^\circ < \alpha < 10^\circ$. In the absence of actuation, the Gurney flap leads to an increase of approximately 0.025 in the downward pitching moment for the entire range of angle of attack. This increase results from the increase in lift near the trailing edge because of the increased suction and pressure on the upper and lower surfaces, respectively. Actuation leads to an increase in the moment coefficient over both the unactuated flap and smooth airfoil (Figure III.3a), resulting in a further reduction in the downward pitching moment. Both the low-pressure domain that forms downstream of the actuator near the trailing edge, and the rise in pressure on the suction surface (Figure III.1) contribute to this effect. For the present airfoil, the center of pressure moves forward with increasing angle of attack (Figure III.3b). In the presence of the inactive hybrid actuator, the center of pressure is $0.05c$ downstream of its location for the corresponding baseline airfoil due to the increased lift near the trailing edge. However, when the actuation is applied, the center of pressure shifts approximately $0.03c$ upstream relative to its position for the baseline airfoil.

III.2 Pulse-Modulated Actuation

III.2.1 Aerodynamic Performance

It is possible to continuously vary the aerodynamic effects of the actuation either by adjusting the amplitude of the (continuous) actuation waveform and thereby the strength of the control jet as measured by its momentum coefficient C_μ (e.g., Amitay et al. (2001)) or by operating the jet on a limited duty cycle (e.g., using amplitude modulation) and therefore effectively reducing its time-averaged momentum coefficient. In the present experiments, the effects of continuous and amplitude modulated actuation waveforms *having the same input power* are compared. Variable duty cycle square wave modulation of the time-harmonic actuation waveform ($f_{act} = 2220$ Hz) is applied at frequencies $5 \text{ Hz} < f_{mod} < 111 \text{ Hz}$.

Figure III.4 shows the variation of the aerodynamic performance of the airfoil at a fixed angle of attack $\alpha = 5^\circ$ over a range of reduced actuation input power (normalized relative to the maximum) q^* and modulation frequency f_{mod} . The figure includes plots of the lift (III.4a), pressure drag (III.4b), L/D_p (III.4c), and C_M (III.4d). In the absence of actuation, i.e. $q^* = 0$, the presence of the inactive Gurney actuator results in a 16% increase in lift over the smooth airfoil ($C_L = 0.408$), and a 34% increase in drag ($C_{Dp} = 0.0143$), corresponding to a decrease in L/D_p of 14% relative to the baseline airfoil (Figure III.4c). As the actuator power is increased, the lift decreases monotonically (cf., Figure III.4a), and, in the case of continuous (unmodulated) actuation, the pressure drag also decreases monotonically so that at maximum power L/D_p increases by 8% relative to the baseline airfoil. However, with modulated actuation the drag decreases to a minimum of $C_{Dp} = 0.0123$ (i.e., 14% less than for the smooth airfoil) for actuation input power in the range $0.8 < q^* < 0.9$ before rising slightly for $q^* = 1$ (i.e. full power without modulation). Figures III.4a and b also show that the variation of the modulation frequency also has a significant effect on the lift and pressure drag coefficients. At low modulation frequencies (e.g. 5 Hz), the variation of lift and drag with increased q^* is similar to the variation observed in the unmodulated case. The decrease in lift and drag *at a constant actuator power level* as f_{mod} is increased to about 40 Hz yields a corresponding increase in L/D_p relative to the baseline airfoil (Figure III.4c) indicating improved actuator performance. For instance, for $f_{mod} = 37$ Hz, the drag is reduced up to 12% compared to continuous actuation, while the lift declines no more than 6%. The effect is most pronounced at lower actuator power levels, particularly at $q^* < 0.4$.

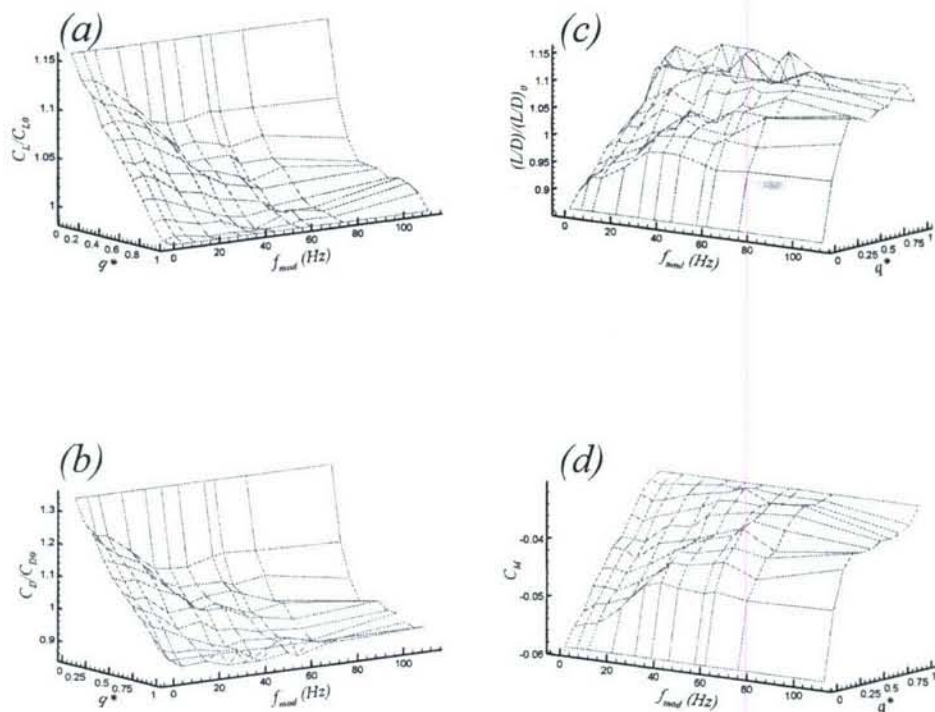


Figure III.4. Variation of (a) C_L/C_{L0} , (b) C_D/C_{D0} , (c) $(L/D)/(L/D)_0$, and (d) C_M with reduced actuation power q^* and modulation frequency f_{mod} , for $\alpha = 5^\circ$. $f_{mod} = 0$ corresponds with continuous actuation.

Further increases of modulation frequency have relatively little effect on aerodynamic performance, except for small increases in the lift and drag at higher actuator power levels. Figure III.4c shows that L/D_p has a maximum for $q^* \sim 0.8-0.9$ and f_{mod} around 40 Hz because of the minimum drag that occurs under the same conditions (Figure 6b). In particular, for $f_{mod} = 37$ Hz and $q^* = 0.9$, L/D_p is 8% greater than for continuous actuation at $q^* = 0.9$, and 6% greater than in the case of continuous actuation at full power. Finally, the variation of pitching moment coefficient C_M with f_{mod} and q^* is shown in Figure III.4d. The pitching moment is most negative in the unforced case, and increases monotonically with actuator power. As modulation frequency is increased, the moment coefficient for a given power level increases from its value at $f_{mod} = 0$ to a peak at f_{mod} around 60 Hz and changes little at higher frequencies, except at higher power levels where there is a slight decrease in C_M under some conditions.

This (limited) parametric data suggests that intermittent (or modulated) operation of the actuator can yield aerodynamic performance improvements that are higher than what is achievable with continuous actuation at the same input power levels. As shown in §III.2.2 below, these changes are associated with transient effects that occur during the activation and deactivation of the actuation and are not present during continuous operation. The advantages of transient actuation in other aerodynamic flow control configurations was explored in earlier work at Georgia Tech, e.g. Amitay and Glezer (2002).

III.2.2 The Flow Field Near The Trailing Edge

The flow field in the vicinity of the airfoil's trailing edge (with the hybrid actuator installed) is investigated using particle image velocimetry (PIV) in a cross stream plane that is normal to the sweepplane. Each measurement domain is comprised of eight partially overlapping frames each having a field of view measuring 40.6 x 41.2 mm. Each frame is computed from an ensemble of 500 realizations (image pairs). Maps of vorticity distributions and cross stream velocity vectors in the streamwise domain $0.88 < x/c^* < 1.13$ are shown in Figure III.5 ($\alpha = 4^\circ$). Because the view is normal to the sweepplane, the x -coordinate is scaled by $c^* = c \cdot \cos \gamma$ (where γ is the sweep angle). The flow in the absence of actuation is shown in Figure III.5a, while in Figures III.5b and III.5c actuation is applied at 50% power of the continuous (unmodulated) actuation waveform and with modulation at 50% duty cycle and $f_{mod} = 37$ Hz, respectively. As shown in §III.2.1, at these actuation levels, L/D_p is 2% lower and 4% higher than for the baseline (smooth) airfoil, respectively. Recall that as shown in §III.1, performance improvements up to 20% in L/D_p can be achieved using the hybrid Gurney flap actuator.

In the absence of actuation (Figure III.5a) a domain of recirculating separated flow is formed downstream of the actuator and extends beyond the trailing edge of the airfoil with a stagnation point that is off the surface, at $x/c^* = 1.018$ and $y/c^* = -0.013$. Some vorticity from the upstream boundary layer is trapped in this domain, while there is still vorticity flux into the wake beyond its edge. When the actuator is operated at 50% continuous power in the absence of modulation (Figure III.5b), the recirculation domain contracts significantly as a result of the interaction with the jet. The reduction in the local pressure is accompanied by a reduction in the extent of the trapped CCW vortex (note the formation of CW vorticity on the upright surface of the actuator), improved attachment near the trailing edge and the upstream migration of the stagnation point to

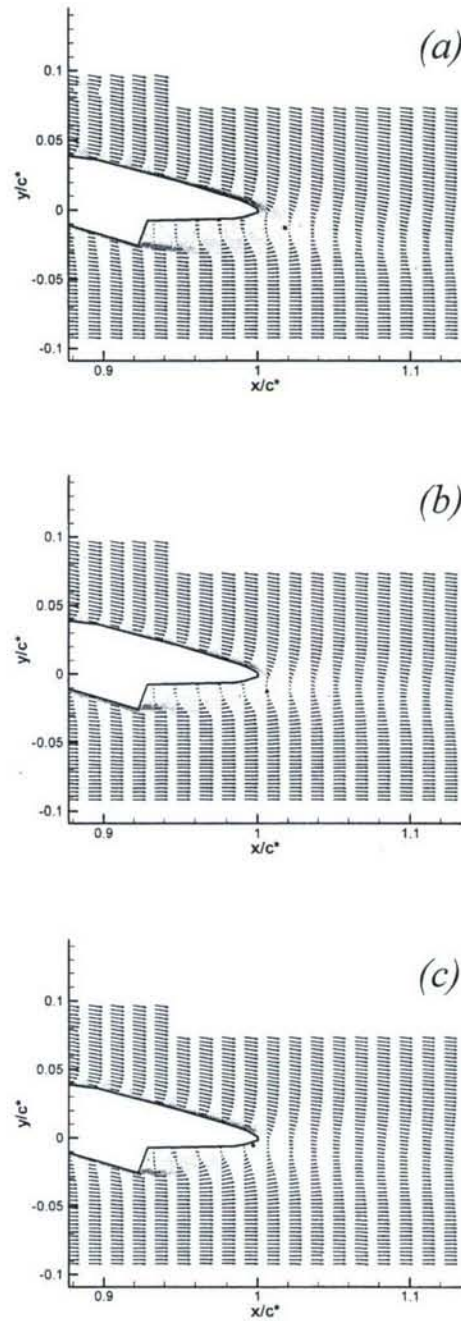


Figure III.5. Time averaged velocity maps and vorticity contours near the trailing edge in the plane perpendicular to the sweepplane. (a) actuator not operating, (b) continuous actuation at 50% power, (c) modulated actuation, $f_{mod} = 37$ Hz, $q^* = 0.5$. A black circle denotes the stagnation point near the trailing edge.

$x/c^* = 1.006$ and $y/c^* = -0.013$. The changes in the flow near the trailing edge result in pressure recovery (cf., Figure III.1) and there is less downward turning of the flow, resulting in a $0.01c^*$ rise in the center of the wake at $x/c^* = 1.10$. It is also evident that the wake width decreases in the presence of actuation, and the smaller velocity deficit that is associated with a reduction in drag is accompanied by lower vorticity levels. Figure III.5c shows the effects of modulated actuation at 50% duty cycle (but at the same power level as in Figure III.5b). The recirculation domain downstream of the actuator contracts further compared to the continuous actuation (Figure III.5b) and the stagnation point moves closer to the surface to $x/c^* = 0.997$ and $y/c^* = -0.005$. The cross stream width of the wake is increased and the magnitude of the

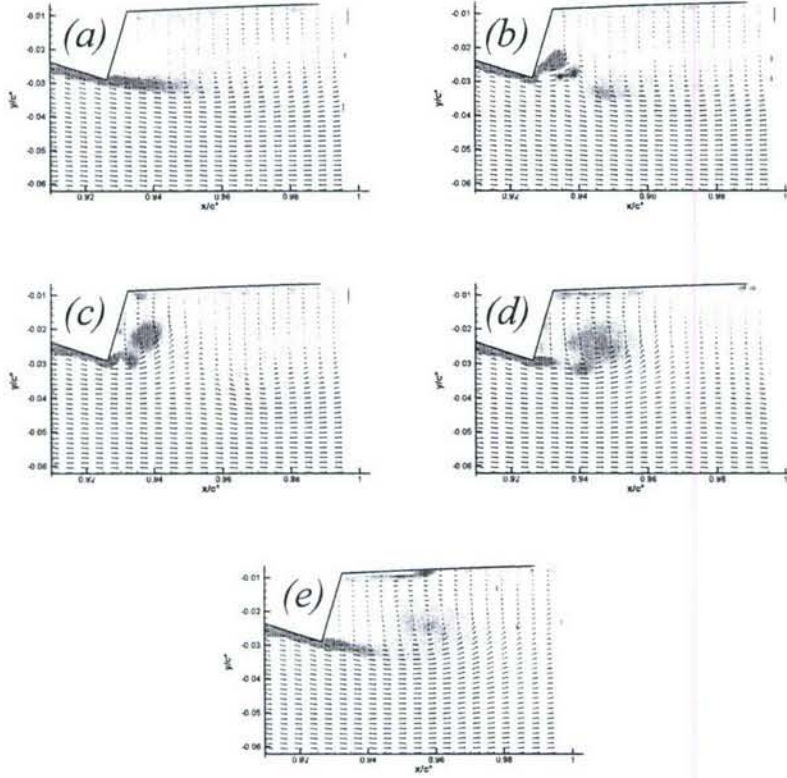


Figure III.6. Phase averaged velocity maps and vorticity contours on the pressure surface near the trailing edge for modulated actuation, $q^* = 0.1$, $f_{mod} = 37$ Hz, for $t/T_{mod} =$ (a) 0, (b) 0.066, (c) 0.13, (d) 0.26, (e) 0.4.

vorticity is lower. This is a result of cross stream oscillations of the wake at the modulation frequency following the onset and termination of the active portion of the modulation cycle.

The transients that are associated with the time-periodic modulation of the actuation waveform lead to variations in lift and therefore shedding of vorticity concentrations of alternating sense when the lift increases or decreases. This process is illustrated by a series of phase averaged vorticity maps near the trailing edge. These data were acquired at 10% duty cycle in order to allow more time for the flow to relax to a pseudo (steady) state, and for the shed vortices to evolve and be advected downstream.

The flow field in the immediate vicinity of the actuator is shown in Figure III.6 at five successive phases of modulation period. The actuator is triggered at the rise of the modulating waveform ($t/T_{mod} = 0$, Figure III.6a). At that time, the flow field near the actuator is similar to the field in the absence of actuation (cf., Figure III.5a) and shows the separated flow domain and the trapped CCW vorticity upstream of the trailing edge. At $t/T_{mod} = 0.066$ (Figure III.6b), a counter rotating vortex pair which is visible near the actuator orifice appears to be advected towards the surface ostensibly as a result of the low pressure domain that is induced by the actuator. The motion of the vortex pair displaces the large CCW vortex farther downstream. It also appears that the CW vortex from the actuator begins to weaken and wrap around the CCW vortex. The remaining phases, $t/T_{mod} = 0.13$, 0.26 , and 0.4 (Figures III.6c, d, and e, respectively), show the evolution of the flow field after the actuation cycle is terminated. As a result of the actuation, a strong CCW vortex is formed immediately downstream of the actuator's edge while entraining CCW vorticity from the upstream boundary layer. As a result, the free stream flow over this segment of the airfoil is turned toward the surface while the CCW vorticity concentration from the previous cycle is shed into the wake. At the same time, the vortex near the actuator continues to grow towards the trailing edge and persists until the next actuation cycle.

A more global view of the flow near the trailing edge is shown in Figure III.7 which is a sequence of three phase-averaged composite images during and following the actuation cycle. In Figure III.7a ($t/T_{mod} = 0.06$), the actuator is still active and two successive vortex pairs are visible in the image. Because of the predominantly CCW vorticity in the upstream boundary layer and the direction of the cross flow, the CCW vortex weakens and diffuses rapidly. It is noteworthy that because the flow is effectively unactuated 90% of the time, the wake is still turned downward. Following the completion of the actuation cycle $t/T_{mod} = 0.16$ (Figure III.7b), the vorticity that is trapped by the jet from the upstream boundary layer begins to roll up and displaces the earlier vorticity concentration into the wake. At the same time, the near wake

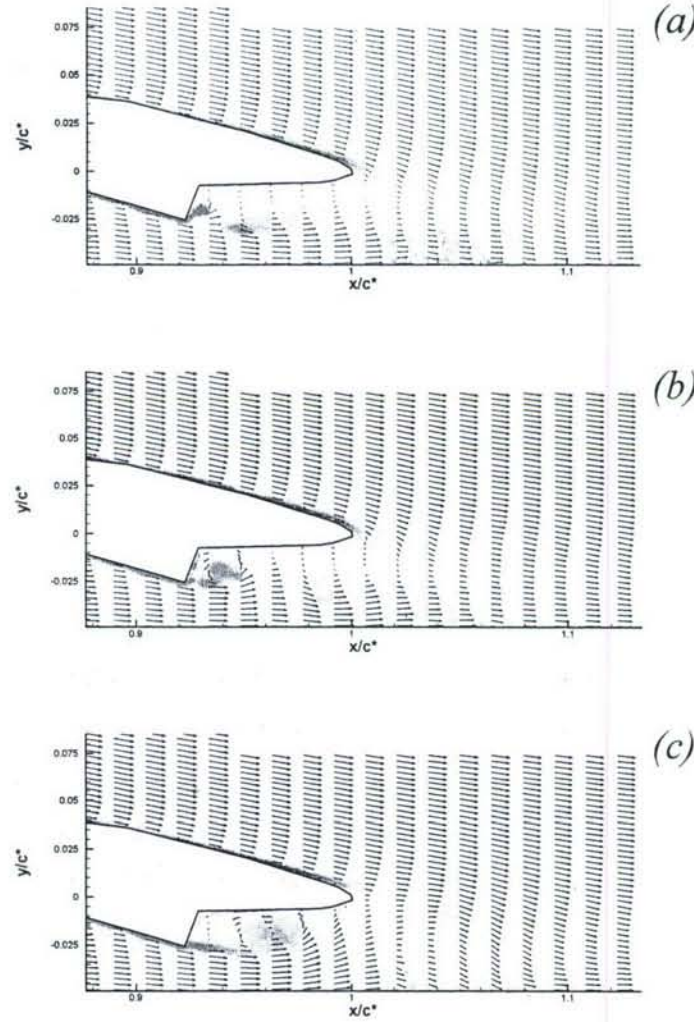


Figure III.7. Phase averaged velocity maps and vorticity contours for modulated actuation, $f_{mod}=37$ Hz, $q^*=0.1$, for $t/T_{mod} = (a) 0.06, (b) 0.16, (c) 0.42$.

downstream of the trailing edge is beginning to turn upward. This process continues and at $t/T_{mod} = 0.42$ (Figure III.7c), the new CCW vortex is rolled up and virtually no CCW vorticity is shed into the wake indicating the trapping of a new vortex. The vorticity then continues to accumulate for the remainder of the cycle until the actuator is operated again.

It is clear that the shedding of vorticity concentration during the modulation cycle leads to variations in circulation about the airfoil. In order to assess the variation of circulation over time, the (phase-averaged) time-periodic changes in vorticity flux past the location $x/c^* = 0.997$ on the pressure side of the airfoil are computed from a sequence of phase-averaged PIV images of the

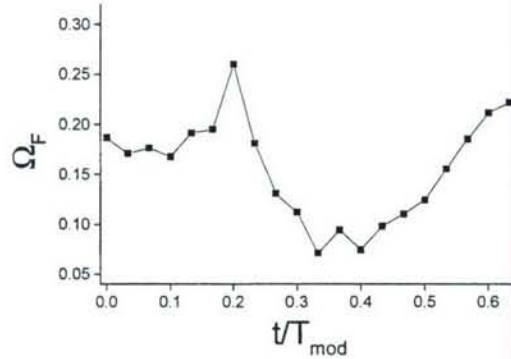


Figure III.8. Variation of scaled vorticity on the pressure side of the airfoil flux past $x/c^* = 0.997$ with time, scaled by modulation period.

flow field (Figure III.8). Contributions from the fluctuating components of velocity and vorticity are neglected. During the early phases of the modulation cycle, up to $t/T_{mod} = 0.13$, several counter rotating vortex pairs form at the jet orifice and migrate downstream while displacing the existing large CCW recirculating domain from the previous cycle. (Figure III.7) The movement of the CCW vortex past the trailing edge leads to a positive peak in the flux at $t/T_{mod} = 0.2$. The removal of the large CCW recirculating domain and formation of a new smaller CCW vortex downstream of the actuator cause the freestream to be drawn toward the surface (cf., Figure III.7b) and results in a substantial reduction in the vorticity flux at $0.25 < t/T_{mod} < 0.55$. This process is followed by the slow buildup and downstream migration of the new CCW recirculation region, which continues for the remainder of the cycle.

The changes in the structure of the wake as a result of continuous and modulated actuation at equal power input are assessed from cross stream distributions of the velocity and Reynolds stresses in Figure III.9 averaged over the region $1.33 < x/c < 1.43$. The cross stream velocity distributions in Figure III.9a show that in the absence of actuation, the wake is deflected downward ($y = -0.08c$) as a result of the increase in lift (cf., §III.1) with a width of $0.13c$ between points of $0.99U_\infty$. When continuous actuation is applied, the wake becomes noticeably narrower ($0.10c$) and is deflected upward (its centerline is at $y/c = -0.05$), and there is a 2% decrease in the velocity deficit, indicating a reduction in drag. However, when the actuation waveform is amplitude-modulated, the time-averaged wake becomes significantly wider ($0.18c$) and the velocity deficit is reduced by 33% compared to the continuous actuation. As noted in §III.2.1, at the same input power level the drag for modulated actuation is lower than for continuous

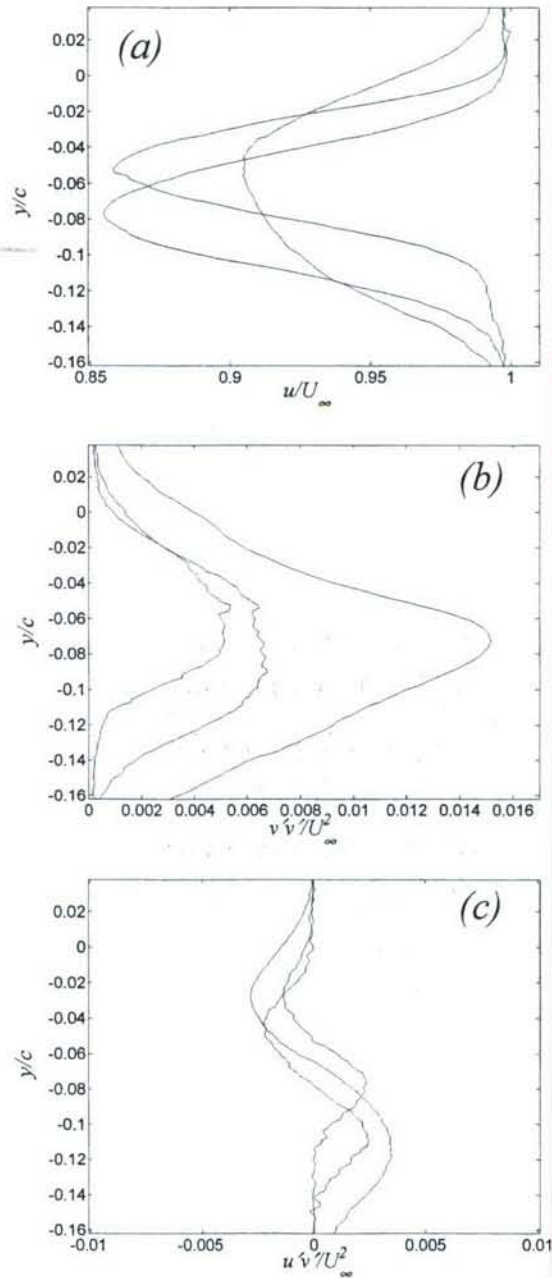


Figure III.9. Time averaged profiles of (a) mean velocity, (b) $v'v'$ and (c) $u'v'$ in the near wake. Unactuated in light gray; continuous actuation at 50% power in gray; square wave modulated actuation at 50% duty cycle in black.

actuation and the spreading of the wake is a result of the shedding of the trapped vorticity. Note that the wake is less symmetric about its centerline (in fact, skewed upward) as a result of the asymmetric shedding of vorticity.

Cross stream distributions of the Reynolds stresses show that continuous actuation leads to a substantial reduction in $v'v'$ compared to the inactive actuator and a decline in $u'v'$ on the suction surface, along with a shift in the turbulence distribution commensurate with the upward shift of the wake. However, the Reynolds stresses are greater in the presence of modulated actuation, due to large scale oscillations of the wake at the modulation frequency. The maximum $v'v'$ for modulated actuation is 125% greater than for the other conditions, and the maximum magnitude of $u'v'$ is 46% larger. This indicates that the contribution to the momentum flux from the velocity fluctuations is greater than in the absence of actuation or for continuous actuation. It is also noteworthy that the maximum $v'v'$ under modulated actuation occurs at $y/c = -0.07$, while the velocity minimum is at $y/c = -0.05$, suggesting that the velocity variation is skewed toward the lower wake, into which the vorticity from the pressure surface of the airfoil is shed.

III.3 TRAPPED VORTICITY CONCENTRATIONS NEAR THE LEADING EDGE

Studies similar to those in the previous section were conducted to characterize the effects on the aerodynamic performance of the airfoil that are engendered by a single hybrid actuator located on the pressure surface near the leading edge. The effects of actuation at various power levels on the pressure distribution and aerodynamic coefficients are analyzed, and flow field measurements in the airfoil boundary layer are used to further characterize the effects of actuation, particularly the effect on wall friction around the entire airfoil. In this configuration the actuator orifice is at $x/c = 0.21$, and at a Reynolds number of $6.7 \cdot 10^5$ the reduced actuation frequency is $St_{act} = 44$. The Reynolds number in these experiments is varied between $6.7 \cdot 10^5$ and $1.3 \cdot 10^6$.

III.3.1 Pressure Drag Reduction

The effect of jet actuation on the pressure distribution around the airfoil when the hybrid actuator is placed at $x/c = 0.21$ is shown in Figures III.10a-c for $\alpha = 4^\circ$ and $Re_c = 6.7 \cdot 10^5$, $1.0 \cdot 10^6$, and $1.3 \cdot 10^6$ respectively. Note that due to the sweep of the airfoil, the flow does not stagnate at the leading edge and therefore the maximum pressure coefficient near the leading edge is on the order of 0.8. As shown in Figures III.10a-c, the local trapped vortex that is formed downstream of the inactive hybrid actuator induces substantial suction and therefore a decrement in C_p within the domain $0.12 < x/c < 0.33$. The maximum magnitude of this decrement increases somewhat with Re_c from (nominally) 0.35 to 0.55. While this reduction in pressure can contribute to a decrease in lift, it is offset by a concomitant, smaller increase in C_p over a larger segment of the pressure surface of the airfoil upstream and downstream of the actuator so that (as shown in Figures III.11 and III.12 below) the net impact on the lift and drag is minimal. It is interesting to note that for $Re_c = 1.34 \cdot 10^6$, the presence of the hybrid actuator leads to an additional reduction in the pressure on the top surface of the airfoil through $x/c = 0.5$.

Actuation of the synthetic jet results in substantial changes in the interaction domain between the actuator and the flow over the pressure surface and evidently in a reduction in the scale and strength of concentration of trapped vorticity. The streamwise extent of the domain in which the pressure decreases is reduced (the downstream edge of this domain moves to $x/c \approx 0.26$), and there is a sharp increase in the magnitude of the maximum pressure decrement. While the extent of the streamwise domain seems to be independent of Re_c , the magnitude of the pressure peak

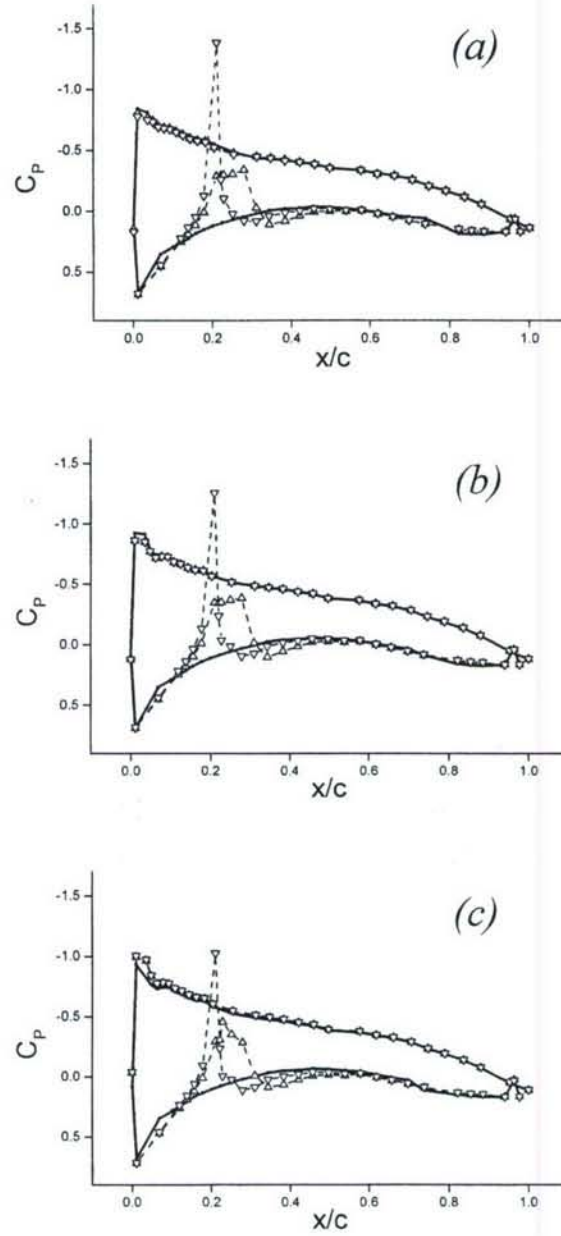


Figure III.10. Pressure distribution around the airfoil for $\alpha = 4^\circ$ for (a) $Re_c = 6.7 \cdot 10^5$, (b) $Re_c = 1.0 \cdot 10^6$, (c) $Re_c = 1.3 \cdot 10^6$. (—) Baseline, (Δ) Actuator not operating, (∇) Actuator operating.

decreases somewhat with increasing Re_c ($C_p = -1.4$, -1.3 , and -1.1). However, it should be noted that in these measurements the actuation amplitude is invariant (to avoid damage to the actuator) and therefore the effective momentum coefficient of the jet decreases with increasing

Re_c (for the data in Figures III.10a-c, $C_\mu = 2.05 \cdot 10^{-3}$, $0.91 \cdot 10^{-3}$ and $0.51 \cdot 10^{-3}$, respectively). As discussed in connection with Figure III.14 below, it is remarkable that the effectiveness of the actuation increases with Re_c and that at $\alpha = 4^\circ$ and $Re_c = 6.7 \cdot 10^5$, L/D_p in the presence of actuation is 2.2 times higher than for the baseline airfoil (96 vs. 43).

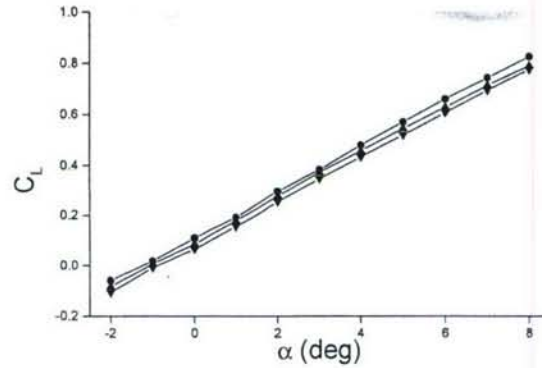


Figure III.11. Variation of C_L with angle of attack. (●) Baseline, (▲) Actuator not operating, (▼) Actuator operating.

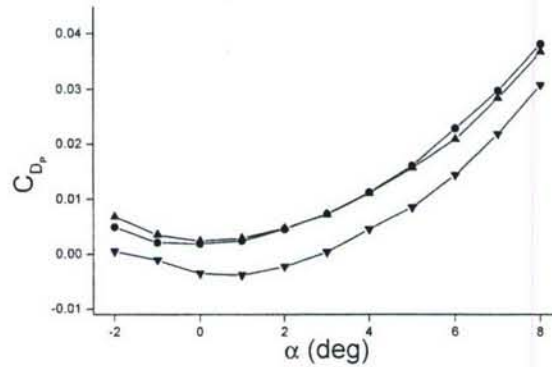


Figure III.12. Variation of C_{Dp} with angle of attack. (●) Baseline, (▲) Actuator not operating, (▼) Actuator operating.

The effects of the actuation on the aerodynamic characteristics of the airfoil for angles of attack within the range $-2^\circ < \alpha < 8^\circ$ are discussed next. The variation of the lift coefficient (Figure III.11) shows that the decrease in pressure on the bottom surface of the airfoil as a result of the presence of the inactive hybrid actuator (cf. Figures III.10a-c) leads to a slight reduction in lift relative to the baseline airfoil which is invariant with angle of attack within the range considered here. The reduction is nominally $\Delta C_L \approx 0.02$ or approximately 4% at $\alpha = 4^\circ$. Jet actuation

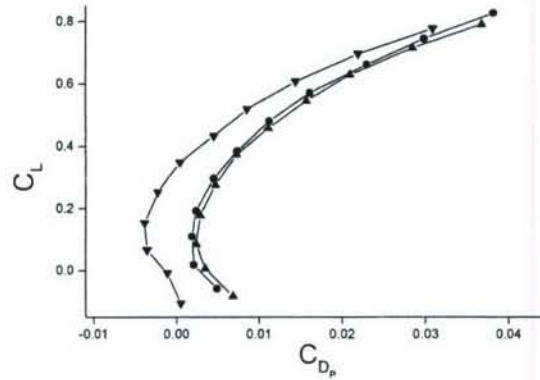


Figure III.13. Pressure drag polar. (●) Baseline, (▲) Actuator not operating, (▼) Actuator operating.

results in additional reduction in lift of 0.02 or $\Delta C_L \approx 0.04$ relative to the smooth airfoil (approximately 8% at $\alpha = 4^\circ$). However, as shown in Figure III.12, the presence of the inactive hybrid actuator results in virtually no change in drag for $1^\circ < \alpha < 5^\circ$, a slight increase for $\alpha < 1^\circ$ and a comparable slight decrease for $\alpha > 5^\circ$. When actuation is applied ($C_\mu = 2.05 \cdot 10^{-3}$), the pressure drag decreases substantially and uniformly (relative to the baseline) over the entire range of α (at $\alpha = 4^\circ$, $\Delta C_D \approx 0.075$). Of particular note are the (small) negative values of C_{D_p} for $-2^\circ < \alpha < 3^\circ$ indicating that the reduction in pressure drag can further offset the friction drag assuming that it is unaffected by the presence of the hybrid actuator (as discussed in §III.3.2). The drag polar for this configuration (Figure III.13) demonstrates that while the curves for the baseline (smooth) airfoil and the airfoil with the inactive hybrid actuators are almost identical, the activation of the jet leads to a shift of the entire curve to the left such that for lowest C_{D_p} attained in the absence of actuation ($C_{D_p} = 0.025$) the lift in the presence of actuation increases from $C_L = 0.08$ to 0.39. In §III.3.2, the friction drag is estimated from boundary layer measurements and it is shown that actuation reduces the total drag from $C_D = 0.017$ for the baseline airfoil to $C_D = 0.012$.

The lift to pressure drag ratio for this airfoil is shown in Figure III.14. As expected, within the range $3^\circ < \alpha < 8^\circ$ L/D_p in the presence of the inactive hybrid actuator is virtually identical to L/D_p for the smooth airfoil while for $\alpha < 3^\circ$ the inactive actuator leads to some degradation in performance. However, jet actuation ($C_\mu = 2.05 \cdot 10^{-3}$) results in a large increase in L/D_p compared to the baseline. The increase at $\alpha = 4^\circ$ is from 42.9 to 96.3 (i.e., over 120%). At lower

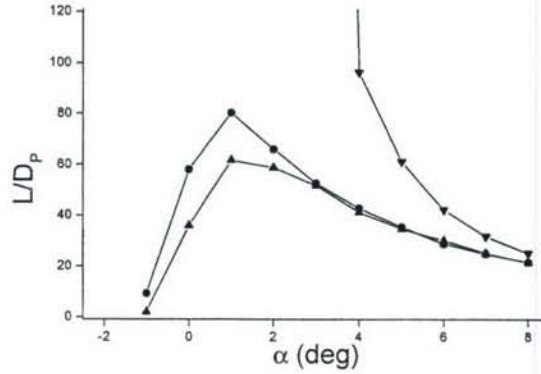


Figure III.14. Variation of L/D_p with angle of attack. (\bullet) Baseline, (\blacktriangle) Actuator not operating, (\blacktriangledown) Actuator operating.

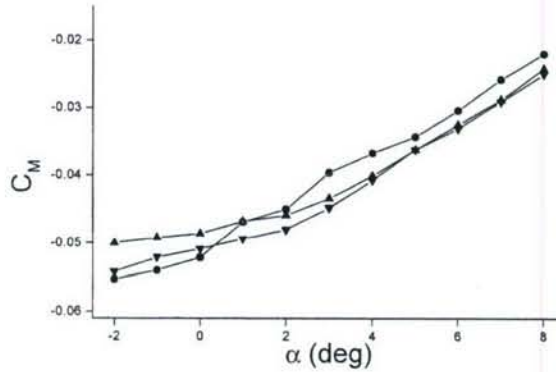


Figure III.15. Variation of C_M with angle of attack. (\bullet) Baseline, (\blacktriangle) Actuator not operating, (\blacktriangledown) Actuator operating.

angles of attack C_{Dp} becomes small and therefore L/D_p is very large. Nevertheless, since the total drag at $\alpha = 4^\circ$ and $Re_c = 6.7 \cdot 10^5$ is known, it is noted that L/D increases from 28.3 for the baseline airfoil to 35.8 for the actuated airfoil, an increase of 27%.

Finally, the effect of the actuation on the moment coefficient (about $c/4$) is shown in Figure III.15 for $1^\circ < \alpha < 8^\circ$. These data show that because of the proximity to $c/4$, the effect of the hybrid actuator in the absence and presence of the jet is rather small. For $\alpha > 3^\circ$ the hybrid actuator results in a slight decrease in C_M (≈ 0.003) where the jet has virtually no effect. For $\alpha < 3^\circ$ C_M for the baseline drops slightly below the moment coefficient of the airfoil with the

inactive hybrid actuator but jet actuation leads to a nominal reduction of 0.003 which brings C_M close to the baseline values.

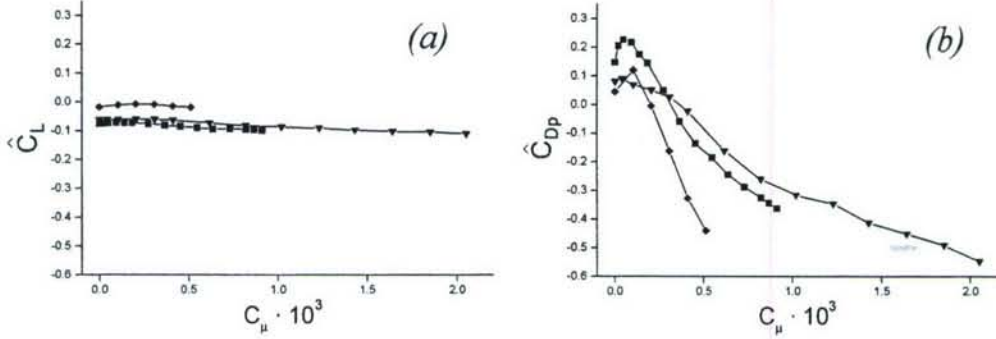


Figure III.16. Variation with C_μ of (a) \hat{C}_L and (b) \hat{C}_{Dp} for $Re_c = (\nabla) 6.7 \cdot 10^5$, $(\blacksquare) 1.0 \cdot 10^6$, $(\blacklozenge) 1.3 \cdot 10^6$.

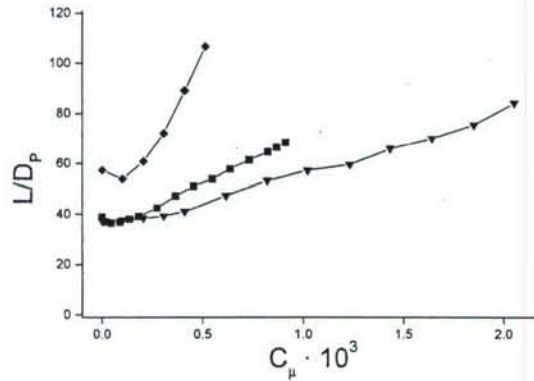


Figure III.17. Variation of L/D_p with C_μ for $Re_c = (\nabla) 6.7 \cdot 10^5$, $(\blacksquare) 1.0 \cdot 10^6$, $(\blacklozenge) 1.3 \cdot 10^6$.

The sensitivity of aerodynamic performance modification to the actuation amplitude as measured by the jet's momentum coefficient is shown in Figures III.16 and III.17 for $\alpha = 4^\circ$ and $Re_c = 6.7 \cdot 10^5$, $1.0 \cdot 10^6$, and $1.3 \cdot 10^6$. Figures III.16a and b show the variation of the fractional lift and drag increments (relative to the baseline airfoil) $\hat{C}_{Dp} = \Delta C_{Dp} / C_{Dp \text{ smooth}}$ and $\hat{C}_L = \Delta C_L / C_{L \text{ smooth}}$. The maximum value of C_μ is limited by the performance of the present actuator. As discussed above, Figure III.16a shows that while the presence of the inactive hybrid actuator results in some reduction in lift, the activation of the jet brings about only a minimal additional change. Overall, the decrease in lift induced by the presence of the hybrid actuator is

less than 10% for $Re_c = 6.7 \cdot 10^5$ and $1.0 \cdot 10^6$, and less than 2% for $Re_c = 1.3 \cdot 10^6$. The corresponding fractional variations in C_D are far more significant. The maximum available C_μ at each of the three Reynolds numbers (in increasing order) results in maximum reductions in pressure drag of 55%, 40%, and 45%, respectively, relative to the baseline configuration. It is interesting to note that at low C_μ (nominally below $0.4 \cdot 10^{-3}$), the jet actuation results in an *increase* in pressure drag relative to the baseline and to the airfoil with the inactive hybrid actuator. It is conjectured that the weak actuation leads to an increase in the extent of the recirculating flow domain downstream of the actuator. Of particular note is the performance at $Re_c = 1.3 \cdot 10^6$ for which the reduction in pressure drag is 45% despite the maximum available jet momentum coefficient of $C_\mu = 0.5 \cdot 10^{-3}$. Figure III.17 shows the variation of L/D_p with C_μ . The most prominent feature of these data is that for a given C_μ (e.g., $0.5 \cdot 10^{-3}$), L/D_p increases with Reynolds number. It is also noteworthy that the L/D_p increases significantly relative to the baseline airfoil when the actuation is active; for $Re_c = 1.0 \cdot 10^6$ and $1.3 \cdot 10^6$, the L/D_p at maximum C_μ increases by 41% and 75%, respectively.

III.3.2 Estimation of Viscous Drag from Boundary Layer Measurements

The evolution of the boundary layer along the airfoil is characterized using high-resolution PIV measurements at a number of stations along its top and bottom surfaces. In addition to detailed velocity distributions and integral measures, it is also desired to estimate of the friction drag and hence the *total* drag from measurement of the (scaled) wall shear stress around the airfoil. The velocity distribution within the boundary layer is measured in cross stream planes that are normal to the spanwise axis of the airfoil at ten streamwise locations on the pressure surface and eight streamwise locations on the suction surface. The fields of view are nominally square and measure between 13 mm and 20 mm on the side. The measurements are obtained at $\alpha = 4^\circ$ and $Re_c = 6.7 \cdot 10^5$. Each data set consists of 400 image pairs. The time-averaged data are used to calculate the displacement thickness, momentum thickness, shape factor, and wall friction coefficient C_f .

The variation of the boundary layer displacement thickness δ^* along the surface of the airfoil is shown in Figure III.18 for the baseline airfoil, and the airfoil with the inactive and actuated hybrid actuator. On the suction surface (closed symbols), the displacement thickness increases monotonically for the three configurations, and is typically slightly (0.1 mm) larger for the

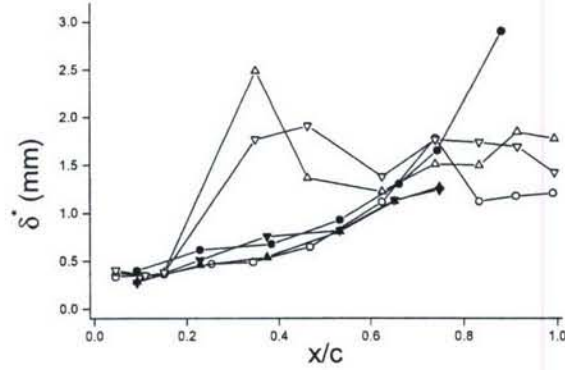


Figure III.18. Variation of δ^* with streamwise location for $Re_c = 6.7 \cdot 10^5$ and $\alpha = 4^\circ$. (●) Baseline, (▲) Actuator not operating, (▼) Actuator operating. Open symbols indicate pressure surface, closed symbols indicate suction surface.

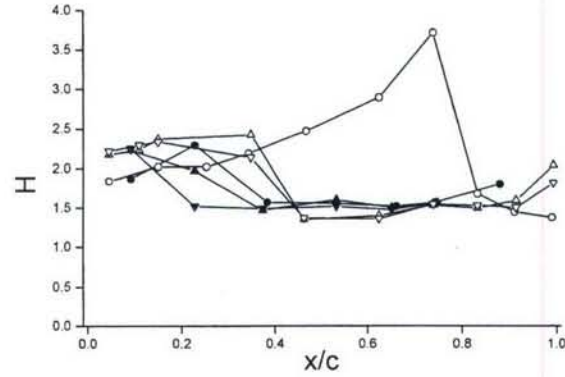


Figure III.19. Variation of boundary layer shape factor with streamwise location. Symbols as in Figure III.18.

baseline airfoil. The presence of the hybrid actuator on the pressure surface of the airfoil leads to a significant increase in δ^* downstream of $x/c = 0.15$ (where $\delta^* \approx 0.37$ mm). The increase in δ^* at the next measurement station (0.13c downstream of the jet actuator orifice), is the result of the formation of the recirculation domain that is associated with the trapped vortex. The effects of this domain are present as far downstream as $x/c = 0.6$. When the actuator is operating, the extent of the recirculating domain is decreased and the magnitude of the displacement thickness is reduced as higher speed fluid is drawn closer to the wall (cf. Figure III.23b). Farther downstream, δ^* remains relatively unchanged at approximately 1.5 mm. The corresponding displacement thickness of the boundary layer of the baseline airfoil increases monotonically up to 0.74c before decreasing to ≈ 1.2 mm after full transition to turbulence.

The state of the airfoil's boundary layer can be assessed from the streamwise variation of its shape factor H (Figure III.19). The values upstream of $0.15c$ on both the top and bottom surfaces are between 1.8 and 2.4, typical of a laminar boundary layer (recall that H is also affected by surface curvature and effects of pressure gradient). There is significant variation in the shape factor on the suction surface near $0.2c$, where the boundary layer appears to undergo transition to turbulence in the presence of the hybrid actuator. Downstream of $0.35c$, a nominal value of 1.5 is measured on the top surface for all three configurations and for both states (i.e., inactive and active) of the hybrid actuator, indicating that the boundary layer downstream of the actuator is turbulent. The shape factor for the pressure surface boundary layer of the baseline airfoil increases monotonically to a level in excess of 3.5 before decreasing to approximately 1.5 near $0.8c$ indicating transition to turbulence. Therefore, it is expected that the friction drag of the smooth airfoil is in fact somewhat lower than in the presence of the hybrid actuator.

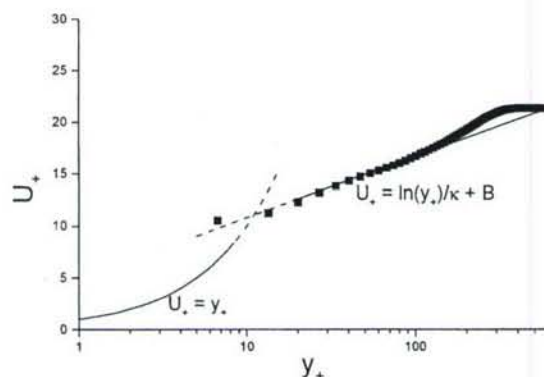


Figure III.20. Cross-stream velocity distribution for a turbulent boundary layer scaled to fit the universal law of the wall.

The wall friction coefficient C_f is computed from the measured velocity distributions. At locations where the boundary layer is turbulent, C_f is determined using the method proposed by Clauser (1954) as illustrated in Figure III.20 which shows an example of a cross stream distribution of the streamwise velocity (measured at $x/c = 0.38$ on the suction surface of the airfoil). The measured velocity profiles are scaled to fit the universal law of the wall for a turbulent boundary layer using the wall velocity scale $u_* = [\nu (\partial u / \partial y)_w]^{1/2}$ and the length scale $y u_* / \nu$. The wall friction coefficient is obtained from $C_f = 2(u_* / U_\infty)^2$. Values of C_f using the local external velocity to the boundary layer U_e are also computed. At locations where the

boundary layer is laminar, the velocity distributions are fitted to a Falkner-Skan profile, from which the wall friction coefficient is obtained.

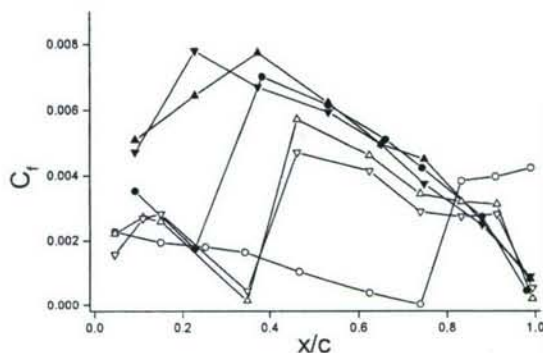


Figure III.21. Variation of wall friction coefficient with streamwise location. Symbols as in Figure III.18.

The streamwise distribution of the wall friction coefficient C_f (normalized by the global free stream velocity) is shown in Figure III.21. On the suction surface (closed symbols), at $x/c = 0.09$ the boundary layer is laminar with $C_f \approx 0.004$. At the next downstream station ($x/c = 0.23$), C_f of the baseline airfoil decreases because the laminar boundary layer continues to develop but then increases (at $x/c = 0.38$) upon transition to turbulence. As noted in connection with the evolution of the shape factor (Figure III.19) transition on the top surface in the presence of the hybrid actuator occurs farther upstream, resulting in larger values of C_f at $x/c = 0.23$. For $x/c > 0.35$, C_f monotonically decreases as a turbulent boundary layer develops, for all three configurations. On the pressure surface (open symbols), the boundary is laminar near the leading edge for all three configurations, with $C_f \approx 0.002$. As noted in connection with Figure III.19, the boundary layer of the baseline airfoil remains laminar as far as $0.74c$ and C_f decreases monotonically with x/c followed by transition and an increase in C_f to ≈ 0.004 . In the presence of the hybrid actuator, C_f decreases significantly downstream of the actuator near the downstream edge of the recirculating flow domain ($x/c = 0.35c$). When the jet is activated the streamwise extent of the recirculating domain decreases and therefore the skin friction coefficient downstream of $x/c > 0.4$ is somewhat lower than with the inactive actuator.

The skin friction drag C_{Df} is estimated from integration of the wall friction coefficient around the airfoil. For the baseline configuration, where the boundary layer is laminar along much of the

pressure surface, $C_{Df} = 0.0058$. In the presence of the hybrid actuator $C_{Df} = 0.0081$ when the actuator is inactive and 0.0076 when the jet is activated. Combining the friction drag with the pressure drag (§III.3.1) yields the total drag coefficient for the airfoil for the three configurations tested here $C_D = 0.0170$ (baseline), 0.0192 (inactive hybrid actuator) and 0.0121 (jet actuation). These results show that for $Re_c = 6.7 \cdot 10^5$, the actuation leads to a reduction of 29% in the total drag relative to the baseline airfoil and therefore to a 27% increase in L/D from 28.3 to 35.8.

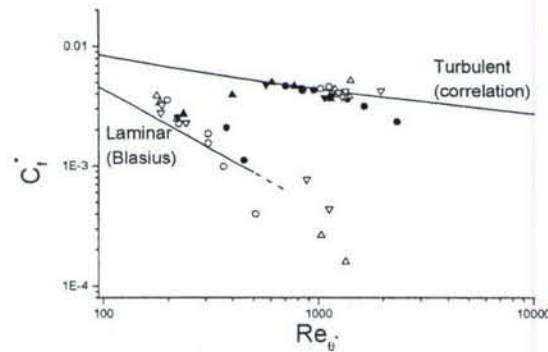


Figure III.22. Variation of C_f^* with Reynolds number based on the boundary layer momentum thickness. Symbols as in Figure III.18.

It is instructive to compare the dependence of the C_f^* , the wall friction coefficient (normalized by the velocity external to the boundary layer) on Re_{θ^*} , (Reynolds number based on the momentum thickness of the boundary layer), as shown in Figure III.22. Also shown are the wall friction coefficient for a Blasius boundary layer, and a correlation for the wall friction of a flat plate turbulent boundary layer (Abbott and von Doenhoff 1959): $C_f^* = 0.306 \ln(4.075 Re_{\theta})^{-2}$. As shown in Figure III.22, the values of C_f^* for the turbulent boundary layers on the surface of the airfoil agree well with the correlation, except in the locations where the flow is not fully attached (i.e., downstream of the actuator and near the trailing edge). When the boundary layer is laminar, the data seems to have the same slope as for the Blasius boundary layer ($n = -1$), but C_f^* is slightly higher ostensibly as a result of the surface curvature and the favorable pressure gradient (corresponding to Falkner-Skan boundary layers where $\beta > 0$).

Finally, Figures III.23a, b, and c show sample cross stream velocity distributions in the pressure surface boundary layer at $x/c = 0.15$, 0.35, and 0.46, respectively. The velocity and cross stream coordinate are scaled by the local external velocity ($U_{e_{sm}}$) and displacement thickness (δ_{sm}^*) of the boundary layer of the baseline airfoil. Note that the velocity between the last valid data point

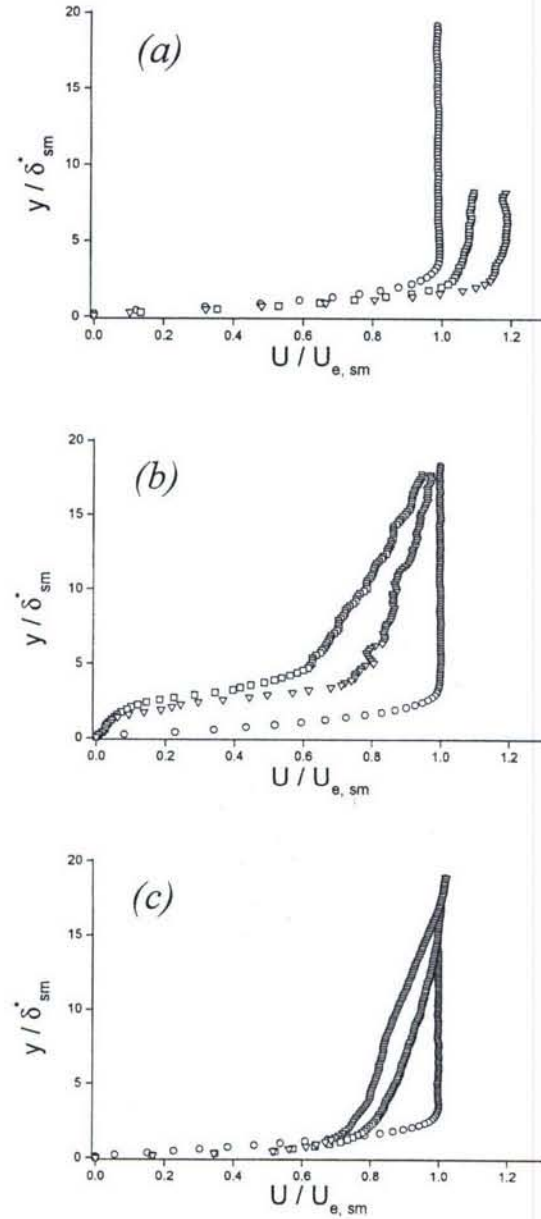


Figure III.23. Cross-stream velocity profiles at $x/c =$ (a) 0.15, (b) 0.35, (c) 0.46. (\circ) Baseline, (\square) Jet inactive, (∇) Jet active.

and the wall is estimated using linear interpolation. Although the velocity distributions upstream of the actuator orifice (Figure III.23a), indicate that the boundary layer of each of the three configurations is indeed laminar, the local external velocity varies significantly and is lowest for the baseline airfoil. The inactive hybrid actuator results in a significant increase of the local external velocity to $1.08 U_{e, sm}$ that is associated with the local reduction in pressure (cf Figures

III.10a-c). The actuation of the jet results in an additional increase in the external velocity to $1.18 U_{e\text{sm}}$ that is apparently commensurate with the large suction peak downstream of the jet (Figure III.10c). Therefore the formation of the trapped vortex domain downstream of the actuator leads to a local acceleration of the external flow and a reduction in the local static pressure that, owing to the slope of the surface, contributes to a significant reduction in the pressure drag (with minimal fractional reduction in lift). It is noteworthy that when the actuator is inactive the extent of the recirculating flow domain is such that the low pressure domain downstream of the actuator nullifies the effect of the reduced pressure upstream. The role of the cross flow in the formation of the trapped vortex and the domain of reduced pressure is evident from similar pressure measurements that were taken in the absence of the cross flow. These measurements have shown that the local change in surface pressure when the jet is actuated at the present momentum coefficient ($C_\mu = 2.05 \cdot 10^{-3}$) is virtually immeasurable.

The velocity distributions in Figure III.23b are measured $0.13c$ downstream of the actuator (the distribution for the baseline airfoil at the same streamwise location is also shown for reference). At this location, the external velocity in the presence of the hybrid actuator (inactive and active) is somewhat lower than the corresponding speed over the baseline airfoil commensurate with the increase in the local static pressure downstream of the actuator compared to the baseline (cf. Figure III.10). Evidently, the reduction in velocity induced by the inactive actuator is considerably larger than when the actuator is active (which reduces the extent of the trapped vortex). For this reason the pressure downstream of the actuator increases when the jet is activated, resulting in a decrease in pressure drag. Further evidence for the pressure recovery is shown in Figure III.23c, where the external velocity downstream of the actuator is almost identical to that of the baseline flow.

IV. BIDIRECTIONAL TRAPPED VORTICITY ACTUATION

Concentrations of trapped vorticity on the pressure and suction sides near the airfoil's trailing edge are used for bidirectional variation of the pitching moment. With one actuator located on the pressure surface near the leading edge ($x/c = 0.21$) and another near the trailing edge ($x/c = 0.94$) the pitching moment is varied continuously over a broad range of angles off attack along with a concomitant reduction in pressure drag relative to the baseline airfoil. The transitory effects associated with pulse modulated actuation are exploited to achieve changes in the aerodynamic characteristics that are similar to continuous (unmodulated) actuation at substantially lower actuation power. Modulated actuation is most effective at modulation frequencies that are commensurate with instabilities of the near wake. The present measurements are conducted at a Reynolds number of $1.0 \cdot 10^6$.

IV.1 Continuous Actuation

The effects of continuous (unmodulated) actuation on the pressure distribution around the airfoil is shown in Figure IV.1 for $\alpha = 4^\circ$ ($Re_c = 1.0 \cdot 10^6$). The pressure distributions are shown for the baseline (smooth) airfoil and the airfoil with both actuators installed in the absence and presence of actuation. It is noteworthy that due to the sweep of the airfoil the flow does not fully stagnate at the leading edge and as a result the maximum pressure coefficient is on the order of 0.8. The effects of the inactive hybrid actuators on the pressure surface on circulation and therefore lift may be thought of as similar to the changes that are associated with the presence of a small trailing edge flap and a leading edge slat or as a change in the effective camber. This is illustrated by the fact that the presence of the actuators results in an increase in pressure of $\Delta C_p \approx 0.15$ on the pressure surface between the actuators and a comparable decrease in pressure across nearly the entire suction surface. The flow accelerates upstream of the front actuator resulting in a local monotonic decrease in pressure between $0.08 < x/c < 0.18$. A domain of (recirculating) trapped vorticity forms downstream of the actuator resulting in a substantial reduction in pressure between $0.18 < x/c < 0.25$. Similarly, the downstream actuator near the trailing edge induces a reduction in pressure upstream of the jet orifice in addition to a decrease in the pressure at the trailing edge (cf. DeSalvo, Amitay, and Glezer 2002).

Continuous operation of both upstream and downstream actuators results in significant alteration of the pressure distribution in the vicinity of each actuator, with relatively little effect on the

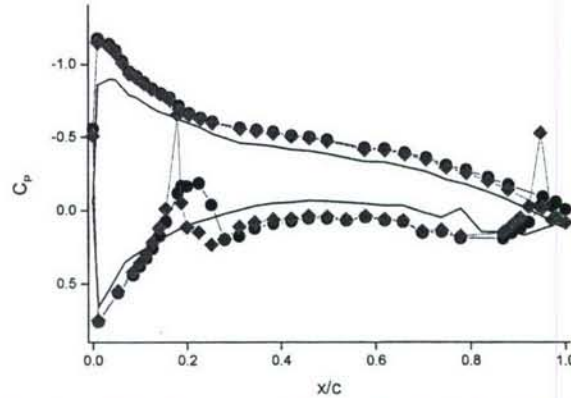


Figure IV.1. Pressure distribution around the airfoil for $\alpha = 4^\circ$ and $Re_c = 1.0 \cdot 10^6$. (—) Baseline, (●) Actuators not operating, (◆) Both actuators operating.

pressure distribution elsewhere on the airfoil (Figure IV.1). A domain of very low pressure is formed near the upstream actuator with a local minimum near the jet orifice where $C_p \approx -0.7$ suggesting an increase in the flow acceleration compared to the unforced flow. Immediately downstream of the actuator, the pressure increases as the trapped vortex diminishes in size due to the reattachment of the separated flow. Between $0.28 < x/c < 0.50$, the pressure due to the actuation is slightly lower when the actuator is inactive but farther downstream this difference vanishes. The downstream actuator effects a local suction peak with a local pressure minimum $C_p \approx -0.5$. The pressure downstream of the actuator and at the trailing edge increases by $\Delta C_p \approx 0.15$, leading to a pressure increase on the suction surface near the trailing edge that extends as far upstream as $x/c = 0.6$ when the actuator is operating. These data show that the changes in pressure that occur due to the operation of either actuator are predominantly local, and it was also shown that the effects of the actuators are relatively independent.

The effects of the actuation on the lift and pressure drag coefficients at various angles of attack are shown in Figures IV.2 and IV.3, respectively for the baseline airfoil and in the presence of the inactive actuators and when either actuator or both are operational. The inactive actuators lead to an increase in lift compared to the smooth airfoil where the lift increment is nearly constant at $\Delta C_L \approx 0.13$ for $\alpha < 6^\circ$. When the downstream actuator is active, the lift increment decreases to $\Delta C_L \approx 0.09$ (relative to the smooth airfoil) regardless of whether the upstream actuator is operational. Perhaps the most important feature of the data in Figure IV.3 is that when both actuators are operational, there is still a net increase in lift of 15% at $\alpha = 6^\circ$ relative to the baseline. When the actuators are inactive, the pressure drag increases by 30% (at $\alpha = 6^\circ$)

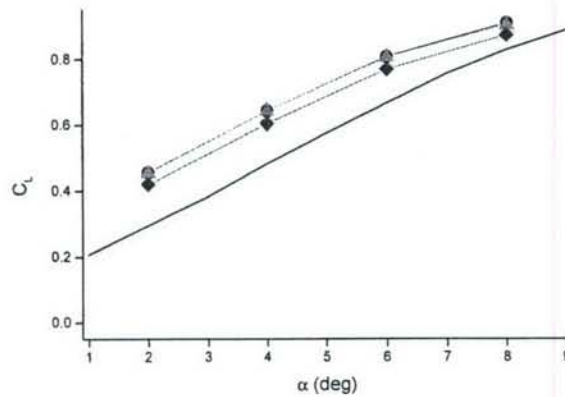


Figure IV.2. Variation of C_L with angle of attack. (—) Baseline, (●) Both actuators not operating, (▲) Upstream actuator only operating, (▼) Downstream actuator only operating, (◆) Both actuators operating.

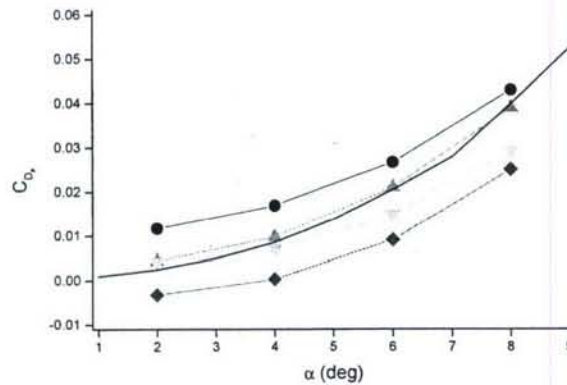


Figure IV.3. Variation of C_{Dp} with angle of attack. Symbols as in Figure IV.2.

relative to the baseline. However, when the upstream actuator (alone) is operating the pressure drag decreases by $\Delta C_{Dp} = 0.005$ and is quite close to the drag of the baseline airfoil. When the downstream actuator alone is active, the drag for $\alpha > 4^\circ$ is less than the drag of the baseline (smooth) airfoil and the magnitude of the drag reduction increases with α . The drag reduction is largest when *both* actuators are operational and it varies from $\Delta C_{Dp} = 0.005$ at $\alpha = 2^\circ$ to $\Delta C_{Dp} = 0.014$ at $\alpha = 8^\circ$. Therefore, the increase in lift and the corresponding decrease in drag lead to an increase in L/D_p by a factor of 2.6 at $\alpha = 6^\circ$.

The pressure drag polar shown in Figure IV.4 is for the three actuation conditions. For a given C_L , operation of either actuator reduces the pressure drag, while operation of both actuators gives the greatest drag reduction and similarly, for a given C_{Dp} , there is an increase in lift when

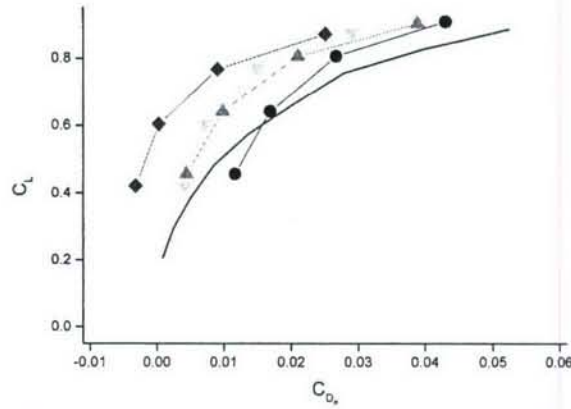


Figure IV.4. Pressure drag polar. Symbols as in Figure IV.2.

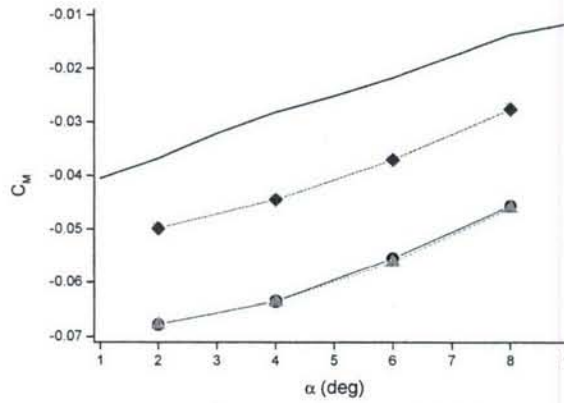


Figure IV.5. Variation of C_M with angle of attack. Symbols as in Figure IV.2.

actuation is applied. For the trailing edge actuator, the pitching moment about $c/4$ (Figure IV.5) increases monotonically with α . When the downstream actuator is inactive, C_M becomes more negative by $\Delta C_M \approx -0.03$ due to the increased pressure and suction on the bottom and top surfaces near the trailing edge. Operation of the downstream actuator reduces the decrement to $\Delta C_M \approx -0.015$ relative to the baseline airfoil. As shown by DeSalvo, Amitay and Glezer (2002), variation of the actuator's momentum coefficient can yield continuous, monotonic change in the pitching moment.

IV.2 Pulse Modulated Actuation

In order to realize the aerodynamic improvements at lower actuation power compared to continuous actuation, it is desirable to utilize pulse-modulated actuation and rely on the global

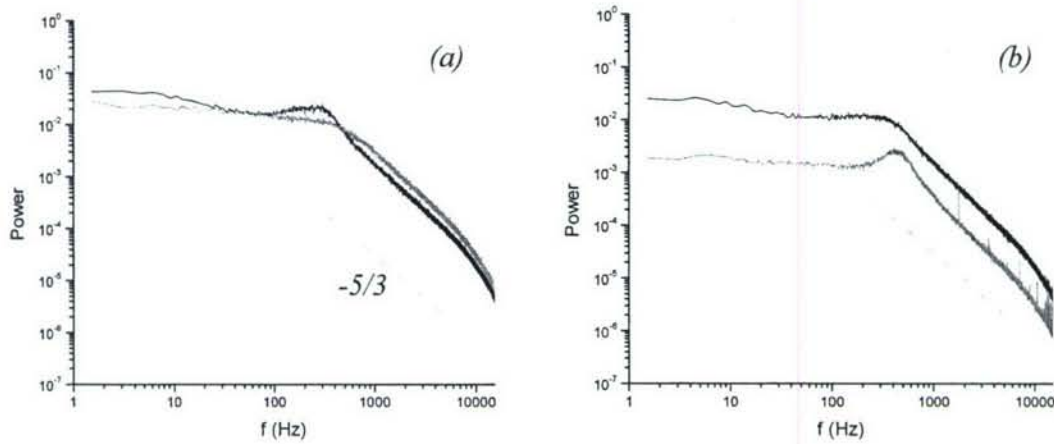


Figure IV.6. Power spectrum of wake $0.25c$ downstream of trailing edge. (a) Upper wake, (b) Lower wake. Actuator not operating is shown in black, continuous downstream actuation in red.

convective time constant of the coupled airfoil/flow system (e.g., Amitay and Glezer 2002) and coupling to the instability of the near wake. The range of receptive wake frequencies (in the absence of stall) is assessed from spectra of the streamwise velocity measured using hot wire anemometry near the upper and lower edges of the wake (Figures IV.6a and b, respectively) at a distance of $0.25c$ downstream of the trailing edge. The unforced spectrum near the top edge shows a discernible frequency band between 150-500 Hz, corresponding to Strouhal numbers (based on the airfoil chord) of 4.1-10 and reduced frequencies based on the characteristic scale of the actuator within the range 0.1-0.2. When the downstream actuator is active, the frequency band vanishes and the spectrum becomes featureless. However, it is remarkable that the response of the pressure surface side of the wake (Figure IV.6b) is different, and the actuation results in an overall reduction in the magnitude of the spectral components and the appearance of a frequency band between 250-600 Hz which is somewhat higher than in the absence of actuation (note also the spectral peaks at the actuation frequency and its higher harmonics within the dissipation range). As shown in Figure IV.12, below, the wake becomes narrower and, the velocity deficit decreases thereby suggesting that its unstable frequency band is somewhat higher. In what follows, pulsed-modulated actuation is at modulation frequencies f_{mod} that are within the receptive band of the wake. The pulse repetition rate is variable, and the pulse duration and phase are adjusted so that the beginning and end of every pulse coincide with zero crossings of the actuator resonance waveform.

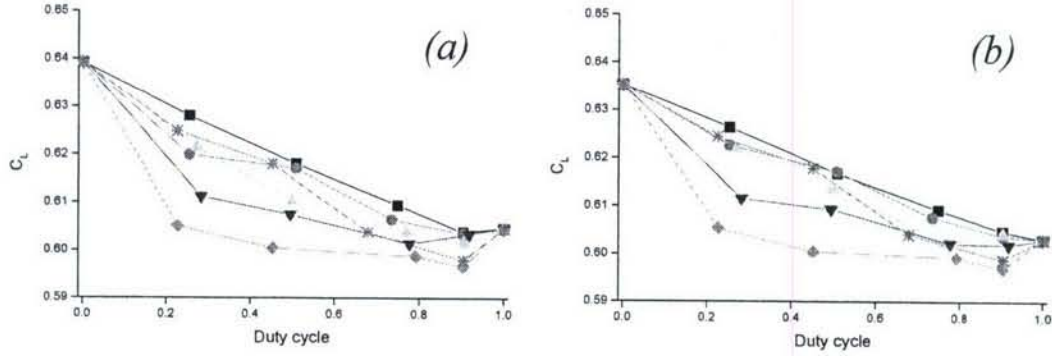


Figure IV.7. Variation of C_L with duty cycle. Upstream actuator (a) inactive, (b) active. Downstream actuator pulse modulated at $St = 0.8$ (■), 1.7 (●), 2.7 (▲), 4.2 (▼), 6.7 (◆), 13.3 (*).

The variation of the lift coefficient with pulse duration and several repetition (modulation) frequencies of the downstream actuator at $\alpha = 4^\circ$ ($Re_c = 1.0 \cdot 10^6$) when the upstream actuator is inactive is shown in Figure IV.7a. The lift coefficient is largest when the downstream actuator is inactive, and decreases monotonically with increasing pulse duration (continuous actuation is achieved when the duty cycle is 1). At the lowest modulation frequency $St = 0.8$ (corresponding to $f_{mod} = 50$ Hz), the lift coefficient decreases almost linearly with pulse duration from $C_L = 0.6393$ until it reaches a minimum of $C_L = 0.6039$ at a duty cycle of 0.9 that is only slightly lower than the level of C_L under continuous actuation. At higher modulation frequencies, the initial rate of decrease of C_L becomes larger and then the rate decrease diminishes. The lowest initial level of C_L is attained when the modulation frequency is $St = 6.7$ which is near the peak of the unstable frequency range of the near wake and the duty cycle is 0.25. It is important to note that at $St = 6.7$, the value of C_L is lowest at a duty cycle of 0.9, with a corresponding $\Delta C_L = -0.04$ relative to the unforced condition, and that C_L has approximately the same value at a duty cycle of 0.25 as under continuous actuation. These variations in lift remain almost unchanged when the upstream actuator is operational (continuously) as shown in Figure IV.7b. These data show that the effect of the upstream actuator on the sensitivity of the lift to pulse modulation by the downstream actuator is minimal (the variation in lift when the upstream actuator is activated is no more than $\Delta C_L = \pm 0.005$).

The corresponding variation of pressure drag coefficient C_{Dp} with modulation frequency and duty cycle is shown in Figures IV.8a and b in the absence and presence of upstream actuation,

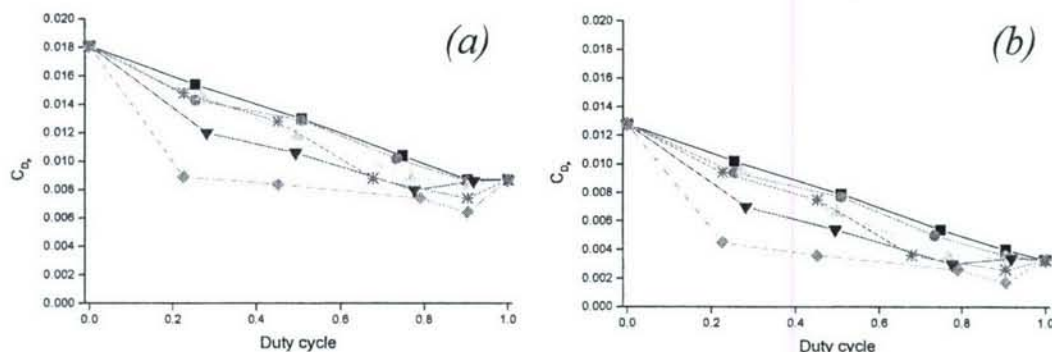


Figure IV.8. Variation of C_{Dp} with duty cycle. Upstream actuator (a) inactive, (b) active. Symbols as in Figure IV.7.

respectively. The trends are similar to the data in Figures IV.7a and b. At low modulation frequencies, C_{Dp} decreases monotonically with increased duty cycle; as the modulation frequency is increased, C_{Dp} decreases with modulation frequency. The lowest drag is attained at a reduced modulation frequency of $St = 6.7$, with a decrease of $\Delta C_{Dp} = 0.009$ at a duty cycle of 0.25. It is important to note that the pressure drag at this actuation condition is almost the same as that of the airfoil with continuous (non-pulsed) actuation, which is also approximately equal to the pressure drag of the smooth (baseline) airfoil. Unlike the variation in lift, when the upstream actuator is activated the pressure drag decreases by $\Delta C_{Dp} \approx 0.006$ (Figure IV.8b), regardless of the operating condition of the downstream actuator. At $St = 6.7$ and a duty cycle of 0.25, the pressure drag is reduced to $C_{Dp} = 0.003$, in comparison to the baseline airfoil pressure drag of $C_{Dp} = 0.009$. Increasing the duty cycle to 0.9 reduces the pressure drag even further to $C_{Dp} = 0.0017$. Compared to continuous actuation of both actuators, with $C_{Dp} = 0.0033$, pulsed modulation of the downstream actuator at a duty cycle of 0.25 (i.e., 25% of the actuation power with the downstream actuator) and $St = 6.7$ with the upstream actuator operating (continuously) results in $C_{Dp} = 0.0045$.

Similarly to Figures IV.7 and IV.8, the variation of the spanwise moment coefficient (about $c/4$) with duty cycle and actuation frequency is shown in Figures IV.9a and b. Continuous operation of the trailing edge actuator leads to a change of $\Delta C_M = +0.017$ relative to the unactuated condition, and pulsed actuation at low modulation frequencies causes C_M to increase monotonically with duty cycle. As the modulation frequency is increased, the moment coefficient becomes less negative for a given duty cycle. The greatest increase in C_M occurs at

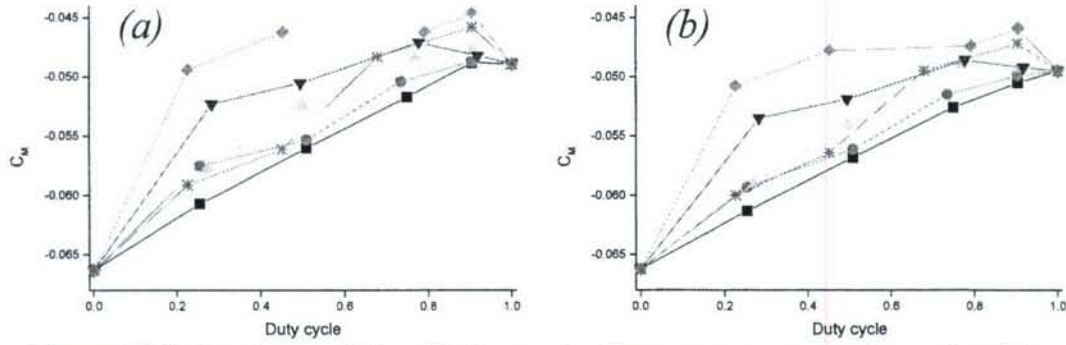


Figure IV.9. Variation of C_M with duty cycle. Upstream actuator (a) inactive, (b) active. Symbols as in Figure IV.7.

$St = 6.7$, for which actuation at a duty cycle of 0.25 gives approximately the same C_M as continuous (unmodulated) actuation. A further increase of $\Delta C_M = +0.004$ can be realized using actuation at a duty cycle of 0.9. Similar to the lift coefficient, activation of the upstream actuator results only in minor change in C_M , as shown in Figure IV.9b because the upstream actuator is located near $x/c = 0.25$.

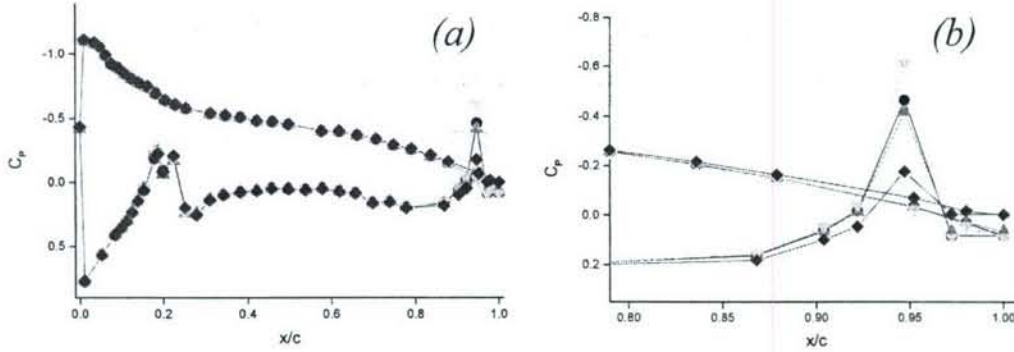


Figure IV.10. Pressure distribution for $\alpha = 4^\circ$ and $Re_c = 1.0 \cdot 10^6$. (a) Global view, (b) detail view. Downstream actuation (●) Continuous, (▲) $St = 1.7$ and 25% duty cycle, (▼) $St = 6.7$ and 25% duty cycle, (◆) $St = 6.7$ and 75% duty cycle.

The effect of modulated actuation of the downstream actuator on the pressure distribution around the airfoil (with the upstream actuator inactive) is shown in Figure IV.10. For $St = 6.7$ and duty cycle 0.25, the pressure distribution is nearly identical to that of the airfoil with continuous (unmodulated) actuation, particularly near the trailing edge as shown in detail in Figure IV.10b. As a result, the aerodynamic forces and moments are similar in these cases. Compared to the case of continuous actuation, operating the actuator at $St = 6.7$ and duty cycle 0.9 causes the pressure minimum near the actuator orifice to strengthen by $\Delta C_p = -0.2$, leading to additional

flow acceleration upstream of the orifice. Downstream of the actuator and near the trailing edge there is a small pressure rise of $\Delta C_p = 0.02$, in addition to a small pressure increase on the suction surface between the trailing edge and $0.85c$. These changes constitute an enhancement of the effects of continuous actuation, leading to an additional reduction in C_{Dp} , decrease in C_L , and increase in C_M . By comparison, actuation at $St = 1.7$ and duty cycle 0.25 generates a weaker low pressure domain near the orifice, resulting in smaller changes in the aerodynamic characteristics as shown in Figures IV.7-9.

IV.3 Circulation Measurements

An analysis of the temporal variation of the aerodynamic characteristics of the airfoil under pulse-modulated and continuous actuation waveforms is conducted using phase-averaged particle image velocimetry (PIV) measurements in the near wake. The phase-averaged velocity field measures 90×90 mm and is centered immediately below the trailing edge of the airfoil $\sim 0.05c$ downstream of the trailing edge. These data are used to compute concentrations of the spanwise vorticity ω_z and thereafter the integral of the vorticity flux across the wake to obtain the global time rate of change of circulation:

$$\frac{d\Gamma}{dt} = \oint_C \omega_z (\bar{\mathbf{v}} \cdot \hat{\mathbf{n}}) dl$$

It is noted that although the integration path C typically surrounds the entire airfoil, the spanwise vorticity normally vanishes everywhere except within the wake. The circulation itself can be obtained from a second integration step.

Figure IV.11 shows the variation of circulation with time when continuous actuation is activated and deactivated at $\alpha = 4^\circ$ and $Re_c = 1.0 \cdot 10^6$ (time is scaled by the convective time scale of the airfoil, $t^* = t/\tau$, where $\tau = c/U_\infty$, and the circulation is scaled by $U_\infty \cdot c/2$). Continuous actuation is initiated at $t^* = 0$ and terminated at $t^* = 2.4$; this is done to provide adequate time for the flow to settle following the change in actuation state. After the initiation of actuation, there is a small increase in the circulation of the airfoil at $t^* = 0.1$ followed by fluctuations, and the primary change in between the unactuated and actuated states begins at $t^* = 0.25$, in which the (scaled) circulation changes by $\Delta\Gamma^* = -0.034$. This change in circulation occurs over a time interval of approximately τ , and is followed by minor fluctuations that decay over the next convective time

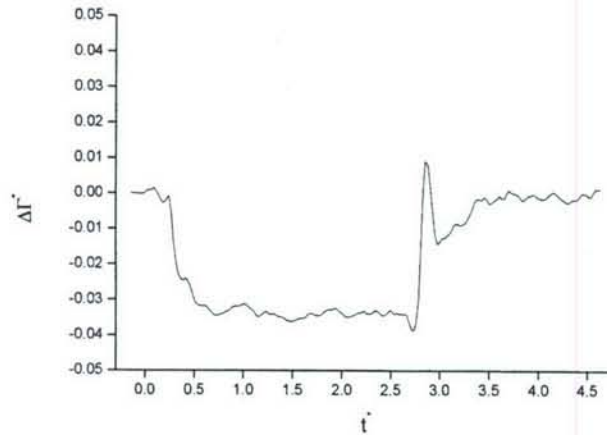


Figure IV.11. Variation of circulation. Continuous actuation of downstream actuator begins at $t^* = 0$ and ends at $t^* = 2.4$.

scale. It is noteworthy that the change in scaled circulation is approximately equal to the change in C_L between the two states (cf. Figure IV.7), using $\Gamma^* = C_L$ for a nominally *steady* flow. However, it is clearly not possible to relate the changes in circulation to the *unsteady* lift during the transient period using the steady formulation. Approximately 0.25τ after the termination of actuation ($t^* = 2.4$), there is another small change in the circulation, followed by a very rapid rise over 0.1τ to a level that is 0.01 greater than the scaled circulation for the airfoil without actuation. The circulation returns to its value for the unactuated airfoil within τ of the termination of actuation. As shown in §IV.1, the actuation also results in substantial reduction in drag. These changes are also apparent in the wake where the maximum velocity deficit is reduced by 13% ($0.1U_\infty$) and the wake width decreases by $\sim 10\%$ as a result of the actuation (Figure IV.12). At the same time, the upward shift in the wake is commensurate with the small reduction in lift.

In general, activations and deactivations of the trailing edge actuator separated by relatively long settling times generate circulation transients of duration $1-2\tau$ after which Γ^* settles to a steady state value. Within the transients, the most rapid circulation changes occur during an interval of duration $0.1-0.25\tau$, which is also in the range of the period associated with the wake receptivity as discussed in connection with Figure IV.6 in §IV.2. These results suggest that it might be possible to drive the transitory changes in actuation (using pulse modulation of the trailing edge actuator on the same timescale as the observed circulation) and thereby couple them to the instability of the near wake so that the desired changes in circulation can be attained at lower actuation power.

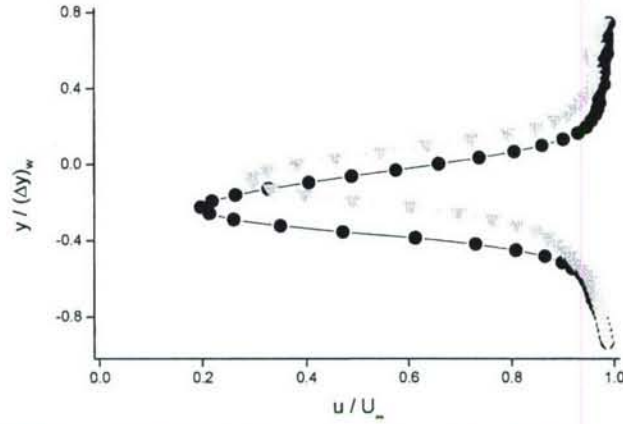


Figure IV.12. Cross-stream velocity profiles of wake. Symbols as in Figure IV.2.

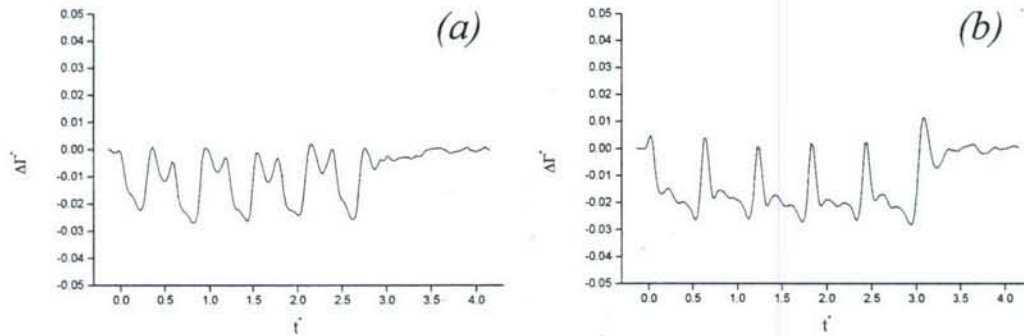


Figure IV.13. Time variation of circulation. Downstream actuation at $St = 1.7$ and duty cycle (a) 0.25, (b) 0.75 beginning at $t^* = 0$ and ending at $t^* = 3.0$.

The variation of circulation following the initiation (at $t^* = 0$) of pulsed modulated actuation of the trailing edge actuator ($\alpha = 4^\circ$ and $Re_c = 1.0 \cdot 10^6$) for $St_{mod} = 1.7$ at duty cycles of 0.25 and 0.75 are shown in Figures IV.13a and b, respectively. In Figure IV.13a (duty cycle 0.25), the actuator is active for 0.15τ and the circulation decreases rapidly following each modulation pulse. When the actuator is inactive (0.45τ), the circulation fluctuates in a manner that is similar to the variation following actuator termination shown in Figure IV.11. Following the initial pulse the circulation changes by $\Delta\Gamma^* = -0.022$ before rising and in subsequent pulses the circulation varies by as much as $\Delta\Gamma^* \approx 0.03$ indicating that there is a longer, global time scale over which the circulation adjusts over the entire airfoil. Following the termination of the modulation pulse train at $t^* = 2.55$, there is a transient change in circulation over the next 0.9τ that is comparable to the changes following the termination of unmodulated actuation as shown in Figure IV.11. When the duty cycle is increased to 0.75 (Figure IV.13b), the actuator is active for 0.45τ and

inactive during the next 0.15τ . It is noteworthy that the nominal change in circulation during each modulation pulse increases slightly with time over the first 2-3 pulses and the circulation increases rapidly and briefly (for $\sim 0.2\tau$) between pulses.

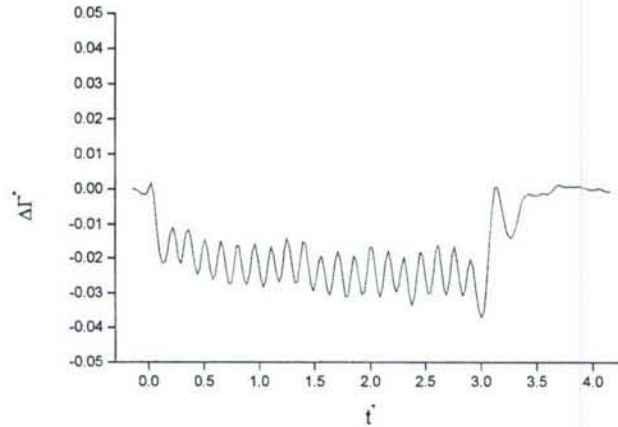


Figure IV.14. Time variation of circulation. Downstream actuation at $St = 6.7$ and duty cycle 0.25, beginning at $t^* = 0$ and ending at $t^* = 3.0$.

The response of the circulation is remarkably different when the modulation frequency is within the receptive band of the near wake. Figure IV.14 shows the effects for $St_{\text{mod}} = 6.7$ at duty cycle 0.25 (period of 0.15τ). This is the modulation frequency for which pulse modulation at duty cycle 0.25 results in nearly the maximum aerodynamic performance at reduced power level. At this duty cycle the circulation oscillates at the modulation frequency but the oscillation amplitude is *lower* than the full excursion that shown in Figure IV.13 ($St_{\text{mod}} = 1.7$) and the nominal mean for $t^* > 1.5$ is $\Delta\Gamma^* \approx -0.025$. As shown in Figure IV.7, the actuation causes the time-averaged lift coefficient to change by $\Delta C_L = -0.035$. These data suggest that by exploiting the interaction of the transients with the flow near the trailing edge it should be possible to tune the modulation frequency such that the amplitude of the oscillating circulation becomes even lower and virtually time-invariant.

The effect of the modulation frequency on the structure of the wake is determined from the time-dependent magnitude and the corresponding cross stream elevation of the maximum velocity deficit (at $0.05c$ downstream of the trailing edge) as shown in Figures IV.15a-f. When the actuation waveform is unmodulated (Figures IV.15a and b), the onset of the actuation at $t^* = 0$ results in a large transitory overshoot deficit decrease from $0.78U_\infty$ to $0.55U_\infty$ which settles

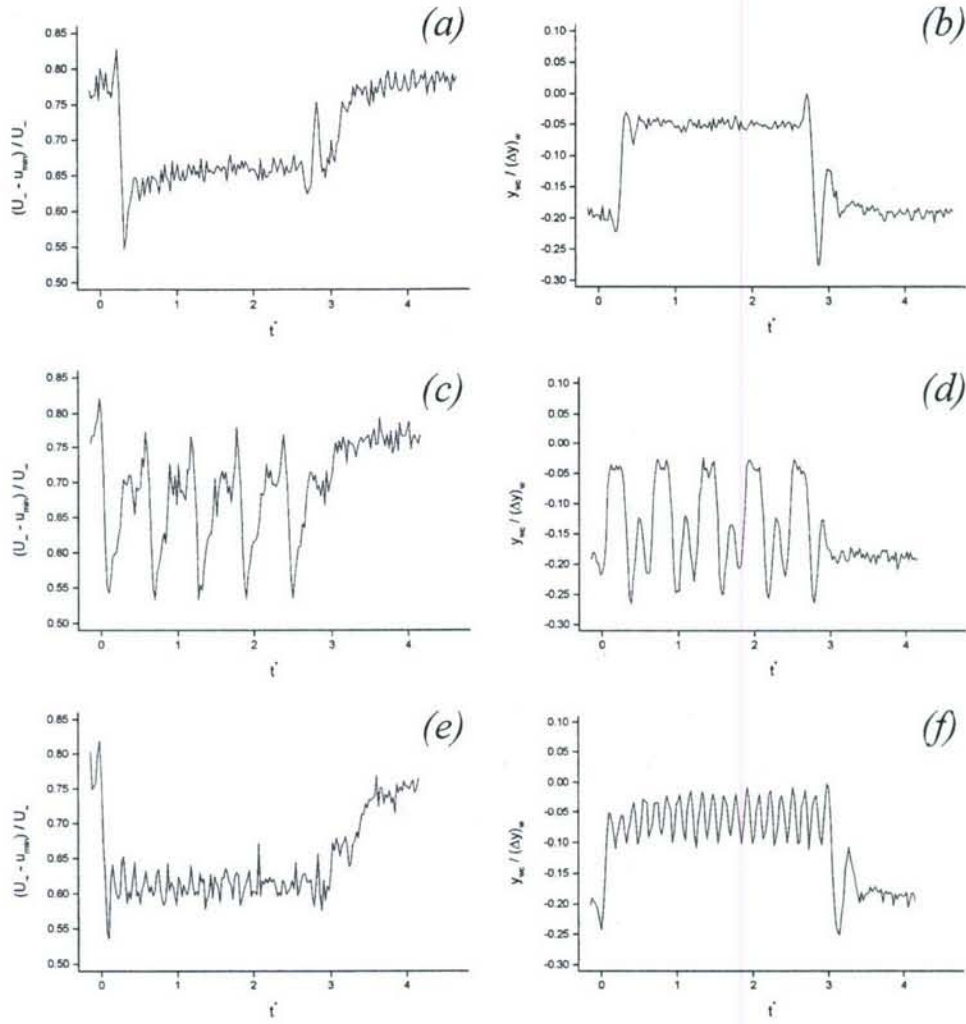


Figure IV.15. Time variation of maximum velocity deficit (a, c, e) magnitude and (b, d, f) location. (a, b) Continuous actuation between $t^* = 0$ and $t^* = 2.4$; (c, d) $St = 1.7$ and 25% duty cycle; (e, f) $St = 6.7$ and 25% duty cycle.

within 1.5τ . Upon termination of the actuation at $t^* = 2.4$, there is another transitory change followed by a settling period that occur on timescales similar to those found during the activation transient. The corresponding time-dependent cross stream elevation of the maximum deficit scaled by the width of the wake $(\delta y)_w$ in the absence of actuation (Figure IV.15b) shows that following the onset of actuation the wake to moves up (i.e., closer to the trailing edge), by $\Delta(y)/(\delta y)_w = 0.15$. When the actuator is deactivated, the wake returns to its original elevation. The time-series of the maximum deficit and its elevation when the actuation waveform is pulse modulated is striking. In Figures IV.15c-d and e-f, the duty cycle is 0.25 and the modulation

frequencies are $St = 1.7$ and 6.7 , respectively. These data clearly demonstrate that as the modulation frequency approaches the locally unstable wake frequency, the magnitude of the oscillations diminishes significantly and the maximum velocity deficit seems to be “locked” to the state that is normally achieved by continuous actuation (e.g., Figure IV.15a). Furthermore, the magnitude of the nominally invariant maximum velocity deficit during the actuation is actually *lower* ($0.62U_\infty$) than when the actuation is continuous ($0.66U_\infty$) and the settling time appears to be shorter.

IV.4 Bidirectional Actuation

The use of two actuators located near the trailing edge of the airfoil enables the pitching moment to be *continuously* varied across a range of values while simultaneously leading to a reduction in pressure drag. These effects are enhanced substantially through the use of pulse modulated operation of both actuators. The effects of activation and deactivation of the actuator (as occurring during pulse modulated actuation) on the nearby vorticity field are investigated, indicating how the creation and manipulation of trapped vorticity near the actuator leads to changes in the airfoil aerodynamic characteristics. The orifice of the pressure surface actuator is located at $x/c = 0.95$, and the suction surface actuator is tested at $x/c = 0.55, 0.75, 0.90$, and 0.95 . Experiments in this section are conducted at a Reynolds number of $Re_c = 1.0 \cdot 10^6$.

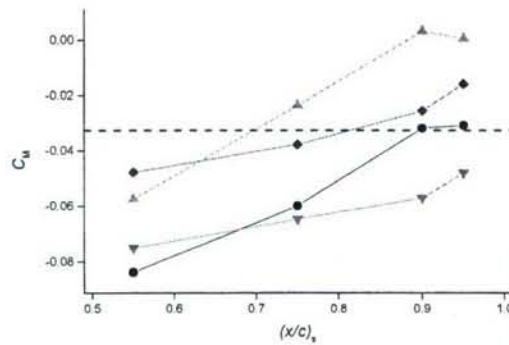


Figure IV.16. Variation of C_M with $(x/c)_s$. (\bullet) Unactuated, (\blacktriangle) Pressure surface actuator operating only, (\blacktriangledown) Suction surface actuator operating only, (\blacklozenge) Both actuators operating, (—) Baseline.

The variations in pitching moment (computed from pressure distributions) at $\alpha = 4^\circ$ are shown in Figure IV.16 when the pressure surface (PS) and suction surface (SS) actuators are simultaneously inactive, and individually and simultaneously active. The coupling between the

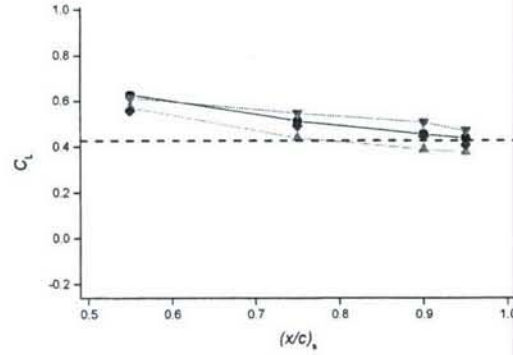


Figure IV.17. Variation of C_L with $(x/c)_s$. Symbols as in Figure IV.16.

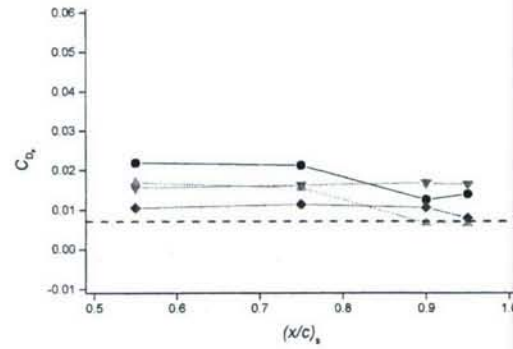


Figure IV.18. Variation of C_{Dp} with $(x/c)_s$. Symbols as in Figure IV.16.

PS and *SS* actuators is evident by the general increase in C_M as the *SS* actuator is moved closer to the trailing edge. Compared to the smooth airfoil (which has a downward pitching moment shown with a dashed line), the pitching moment induced by the *PS* actuator becomes almost positive ($C_M = 0.003$) with the *SS* actuator at $(x/c)_s = 0.90$ where the moment increments between the *PS* and *SS* actuators relative to the smooth airfoil are largest (within the investigated range) namely, $\Delta C_M = 1.10C_{M0}$ and $-0.75C_{M0}$, respectively. Note that simultaneous *PS* and *SS* actuation results in a net pitching moment that is almost the same as for the smooth airfoil. The range of the actuation ΔC_M decreases slightly when the *SS* actuator is placed at $0.95c$, ostensibly as a result of the decrease in the size of the trapped vorticity concentration.

The corresponding changes in lift and pressure drag are shown in Figures IV.17 and IV.18, respectively. It is remarkable that the presence of the *SS* actuator at $(x/c)_s = 0.55$ results in an increment of $\Delta C_L = 0.20$ relative to the baseline, and simultaneously in a substantial increase in

pressure drag $\Delta C_D = 0.015$ in the absence of actuation. These effects diminish as the *SS* actuator is moved downstream. It is noteworthy that when only the *SS* actuator is active, the overall pressure drag is almost invariant regardless of the actuator's streamwise position while operation of the *PS* actuator results in pressure drag that is almost the same as the baseline for $(x/c)_s = 0.9$ and 0.95 . Although C_M can be varied across a wider range of values with the actuator at $0.90c$ than at $0.95c$, the drag penalty due to operation of the suction surface actuator is less with the actuator at $0.95c$; this is particularly true at higher angles of attack, as shown in Figure IV.22b.

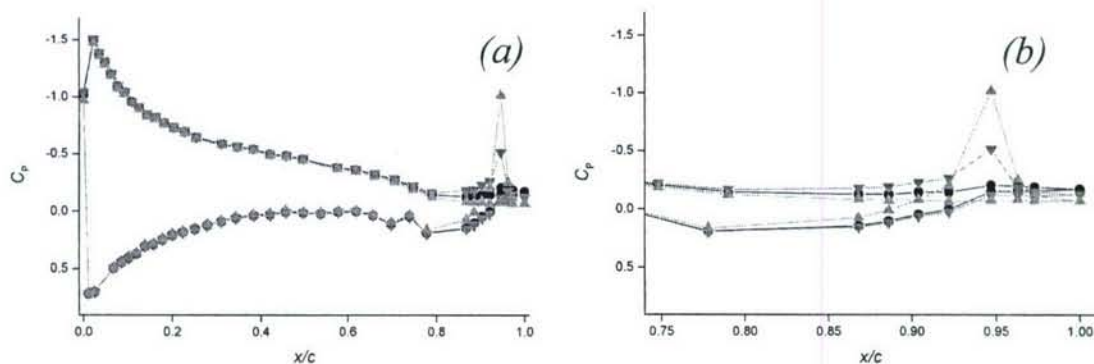


Figure IV.19. Pressure distribution around airfoil at $\alpha = 6^\circ$ and $(x/c)_s = 0.95$. (a) Global view, (b) trailing edge detail. Symbols as in Figure IV.16.

Pressure distributions around the airfoil at $\alpha = 6^\circ$ and $(x/c)_s = 0.95$ (Figure IV.19) show that the operation of the pressure surface actuator leads to a pressure increase at the trailing edge of $\Delta C_p \approx 0.1$ that extends to the opposite surface and therefore leads to a pitch-up moment increment. Similar changes in the pressure distribution occur when the suction surface actuator is operated, producing an opposite, nose-down pitching moment. It is evident that the trapped vorticity concentrations induced by the actuation result in a region of low pressure near the trailing edge that accelerates the flow along both the pressure and suction surfaces of the airfoil. Operation of either actuator causes induces a domain of very low pressure in the immediate vicinity of the actuator, accompanied by an increase in pressure downstream of the actuator and at the trailing edge. As a result, the Kutta condition is manipulated so that the flow on the opposite surface from the operating actuator (around the trailing edge) decelerates, leading to increased pressures and a corresponding pitching moment (cf. Figure IV.16). A further contribution to the pitching moment comes from the reduced pressure immediately upstream of the actuator that is created when the actuator operates.

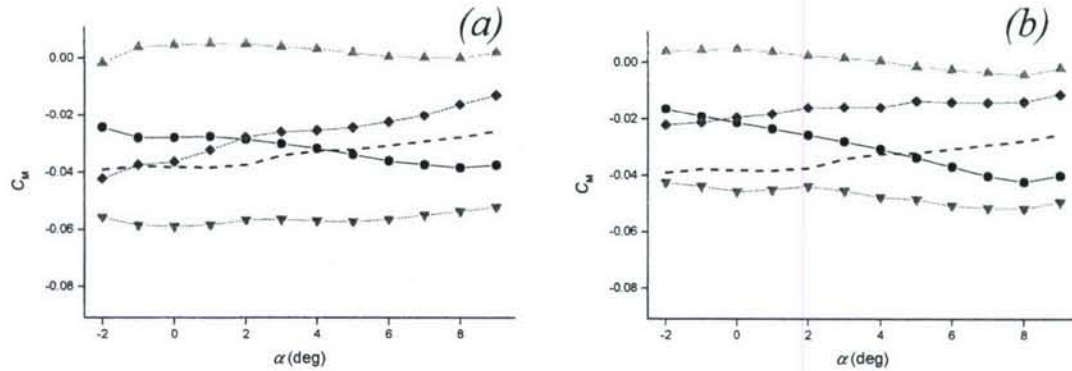


Figure IV.20. Variation of C_M with α for $(x/c)_s = (a) 0.90c$, $(b) 0.95c$. Symbols as in Figure IV.16.

Given the sensitivity of C_M to actuator location (cf. Figure IV.16) and in particular the decrease in drag near the trailing edge, the variation of C_M with angle of attack ($-2^\circ < \alpha < 9^\circ$) was measured at $(x/c)_s = 0.90$ and 0.95 (Figures IV.20a and b, respectively) for the baseline airfoil and in the presence of the inactive and active actuators. The overall trends are similar at both locations. To begin with, in the absence of actuation C_M decreases with α while C_{M0} (for the smooth airfoil) increases with α indicating that the inactive actuators renders the airfoil slightly more stable as evidenced by the change in $dC_M/d\alpha$ compared to the smooth airfoil. When either one of the actuators (*PS* or *SS*) is active, C_M varies only slightly with α . However, while the moment difference between these actuation conditions is also relatively invariant with α ($\Delta C_M = 0.047$ and 0.058 for $(x/c)_s = 0.95$ and 0.90 , respectively), the moment increments induced by *PS* and *SS* actuation relative to the unactuated airfoil monotonically decrease and increase, respectively as α increases. For instance, at $(x/c)_s = 0.95$ and $\alpha = 8^\circ$, ΔC_M (with respect to the unactuated condition) for *PS* and *SS* actuation has respective values of $+0.038$ and -0.009 . The ranges of C_M values that are achievable using actuation alone allow the moment coefficient to be varied between approximately the value of the smooth (unactuated) airfoil and a value corresponding to a (small) nose-up pitching moment. Simultaneous operation of both actuators produces a ΔC_M (with respect to the unactuated condition) of an amount nearly equal to the combination of the ΔC_M values of the individual actuators, indicating that the effects of the *PS* and *SS* actuators on C_M are independent of each other.

The corresponding effects of the actuation on the lift and pressure drag coefficients each measured at $(x/c)_s = 0.90$ and 0.95 are shown in Figures IV.21a and b and IV.22a and b,

respectively. Compared to the unactuated airfoil, operation of either actuator leads to a relative lift increments of $\Delta C_L \approx 0.1$ and 0.12 for $(x/c)_s = 0.9$ and 0.95 , respectively, over the range of angles of attack tested. It is noteworthy that compared to the smooth airfoil, at low α the lift is reduced primarily by the *PS* actuator while at high α the lift increases mostly by the *SS* actuator such that $dC_L / d\alpha$ increases when either actuator is operational. The changes in pressure drag induced by the actuation are shown in Figure IV.22. The presence of the inactive actuators leads to an increase in the cross stream width of the near wake resulting in a substantial increase in C_{Dp}

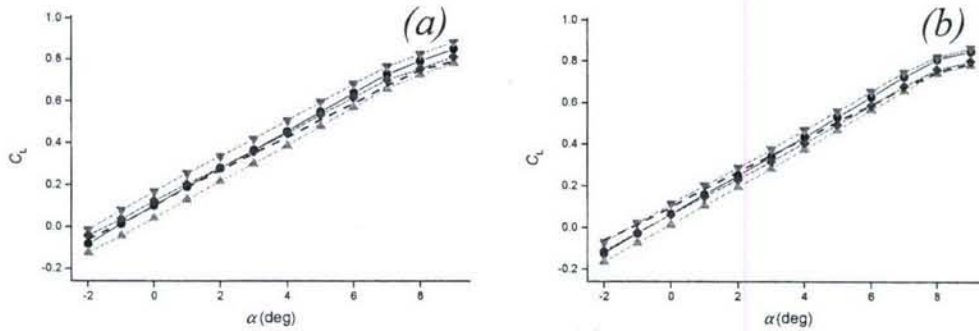


Figure IV.21. Variation of C_L with α for $(x/c)_s = (a) 0.90c$, $(b) 0.95c$. Symbols as in Figure IV.16.

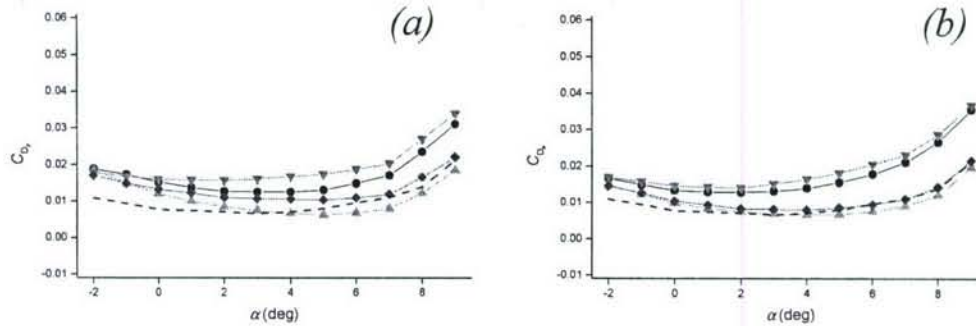


Figure IV.22. Variation of C_{Dp} with α for $(x/c)_s = (a) 0.90c$, $(b) 0.95c$. Symbols as in Figure IV.21.

(50-100% relative to the smooth airfoil). However, as shown in the earlier work of DeSalvo and Glezer (2004), operation of the *PS* actuator can lead to a significant reduction in pressure drag which increases in magnitude with α relative to the smooth airfoil. For example, at $\alpha = 6^\circ$, the pressure drag decreases by 21% when the *SS* actuator is inactive and increases by 17% when the *SS* actuator is active (the latter increase is accompanied by an increase in C_L and a nose down

pitching moment). While the distributions of C_{Dp} at $(x/c)_s = 0.90$ and 0.95 during operation of the *PS* and *SS* actuators are similar, *SS* actuator operation with $(x/c)_s = 0.90$ induces a pressure drag increase of up to 33% compared to only 17% at $(x/c)_s = 0.95$; however, the greater drag penalty is offset by a larger range of C_M values that can be achieved with $(x/c)_s = 0.90$.

IV.4.1 Effects of Transitory Actuation

The earlier works of Amitay and Glezer (2002 and 2006) demonstrated that the aerodynamic performance of separated flows that are typically controlled by continuous actuation can be substantially improved by actuation of transitory vortical structures using pulse-modulated actuation. The modulating frequency of the actuation waveform f_{mod} is related to the global convective time scale of the flow. Recently, DeSalvo and Glezer (2006) showed that this approach can also be applied for trapping and regulation of vorticity concentrations at low angles of attack when the baseline flow is fully attached. In particular, when the modulation frequency was coupled to an instability of the near wake, improved aerodynamic performance (e.g., reduction in pressure drag) could be achieved at substantially lower actuation power. These effects were investigated over a broad range of operating conditions in the context of the present work.

The transitory aerodynamic performance of the airfoil is first characterized using step- and pulse-modulation of the actuation waveform. The evolution of the flow field near the trailing edge is assessed from phase-averaged particle image velocimetry (PIV) where the field of view measures 140×140 mm and is centered about a location $0.05c$ downstream of, and at the same vertical position as, the trailing edge. These data are used to compute the spanwise vorticity concentrations ω_z and thereafter the integral of the vorticity flux across the wake to obtain the global time rate of change of circulation $d\Gamma/dt = \oint_C \omega_z (\bar{\mathbf{v}} \cdot \hat{\mathbf{n}}) d\mathbf{l}$. It is noted that although the integration path C typically surrounds the entire airfoil, the spanwise vorticity normally vanishes everywhere except within the wake, and thus the time rate of change of circulation for the entire airfoil can be deduced from an analysis of the wake. The circulation itself is obtained by integration.

The temporal evolution of the near wake following a switch between the two actuators (i.e., step deactivation of the *PS* actuator and simultaneous step activation of the *SS* actuator) is inferred from a series of phase-averaged cross-stream distributions of streamwise velocity and spanwise

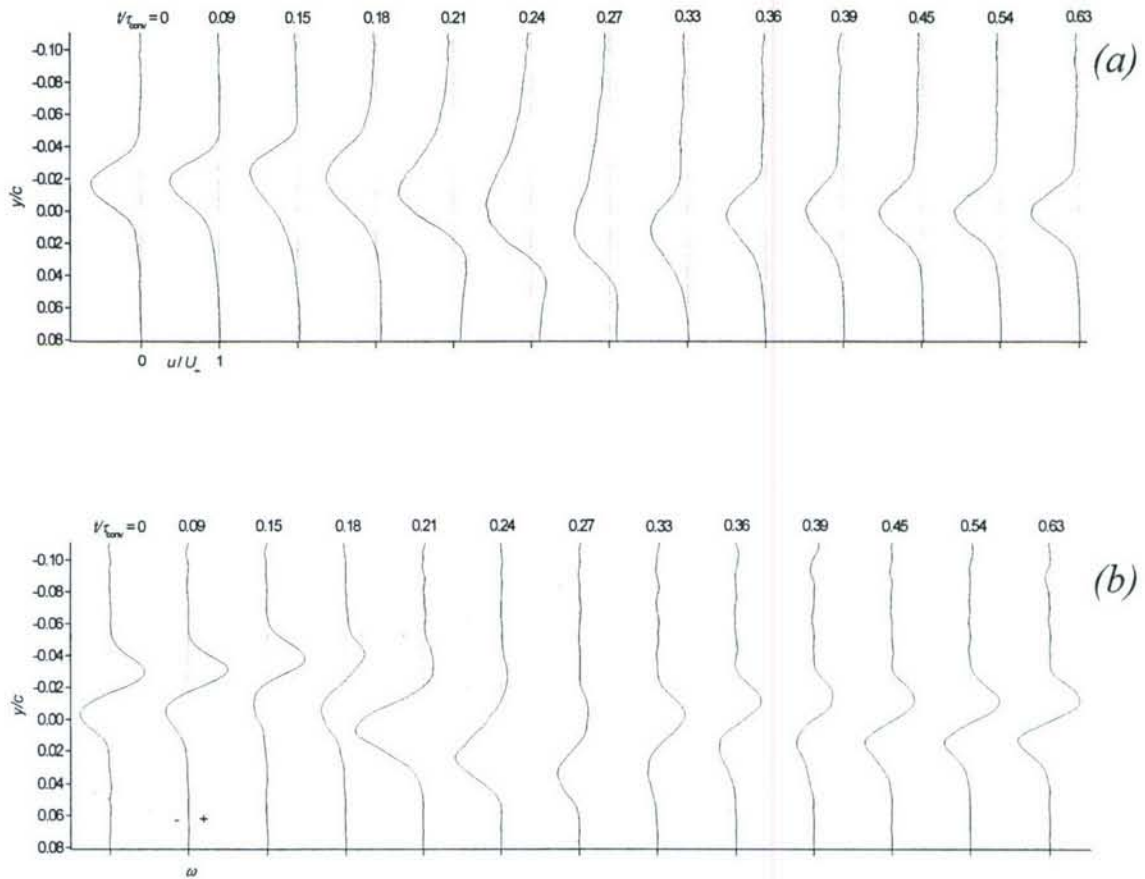


Figure IV.23. Wake profiles following transition from pressure surface to suction surface actuation at $t/\tau_{conv} = 0$: (a) streamwise velocity, (b) spanwise vorticity.

vorticity measured $0.09c$ downstream of the trailing edge at $\alpha = 4^\circ$ (Figures IV.23a and b, respectively). Before the *PS* actuation is terminated (at $t/\tau_{conv} = 0$, where $\tau_{conv} = c/U_\infty$ is the characteristic convective time scale) and while the *SS* actuator is inactive, the wake has a nominal width of $0.09c$ and maximum velocity deficit of $0.63U_\infty$. The simultaneous respective activation and deactivation of the *SS* and *PS* actuators leads to a brief, upward tilt of the wake ($\Delta y = +0.005c$ between $t/\tau_{conv} = 0$ and 0.15), followed by broadening of the lower segment of the wake. It is noteworthy that while initially ($t/\tau_{conv} = 0$) the cross stream distribution of spanwise vorticity (Figure IV.23b) is almost symmetric about the wake centerline (even though the bottom, *PS* actuator is active), the wake tilt and broadening are accompanied by a reduction in the magnitude of the CCW (negative) vorticity layer associated with the pressure side of the airfoil

that is followed by a substantial increase in concentration of CCW vorticity at $t/\tau_{\text{conv}} = 0.21$ as vorticity trapped by the *PS* actuator is released and shed into the wake. At the same time, following the activation of the *SS* actuator, it appears that flux of CW (positive) vorticity from the suction surface is momentarily reduced indicating accumulation downstream of the actuator and is indicative of an increase in lift (cf. Figure IV.21). During these changes in vorticity concentrations, the wake tilts toward the pressure surface by as much as $\Delta y = -0.035c$ (relative to the cross stream position at $t/\tau_{\text{conv}} = 0$) at $t/\tau_{\text{conv}} = 0.27$. Subsequently, the wake begins to recover from the transients associated with the change in actuation, tilts upward, regains its symmetry, and the vorticity fluxes from the top and bottom surfaces of the airfoil become approximately equal. In its final stable form, as shown at $t/\tau_{\text{conv}} = 0.63$, the wake is displaced toward the pressure surface by $\Delta y = -0.020c$ relative to its cross stream position at $t/\tau_{\text{conv}} = 0$ and has the same nominal width.

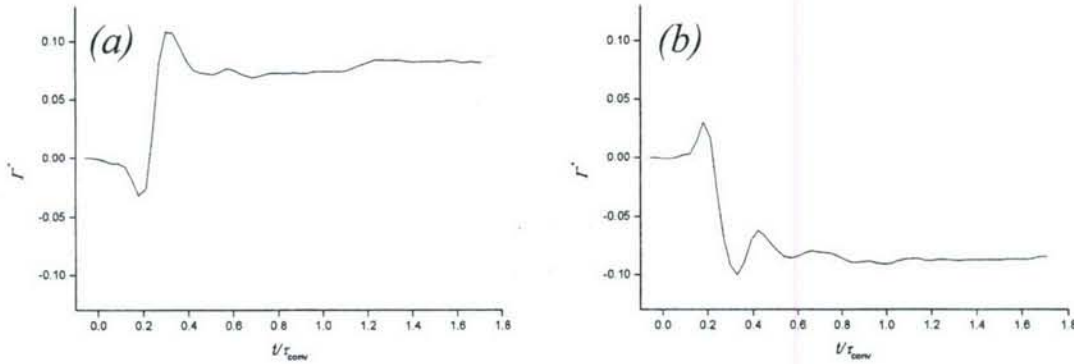


Figure IV.24. Circulation. Actuation changing from (a) pressure surface to suction surface, (b) suction surface to pressure surface.

Transitory changes in the normalized circulation around the airfoil $\Gamma^* = \Gamma / (U_\infty \cdot c/2)$ (calculated from the vorticity flux) when the actuation is switched between the *PS* and *SS* actuators are shown in Figure IV.24. When the actuation is switched from the *PS* to *SS* actuators (Figure IV.24a), the rise in circulation is preceded by a small decrease at $t/\tau_{\text{conv}} = 0.12$ which occurs as a result of a momentary accumulation of CCW vorticity near the *PS* actuator while shedding of CW vorticity from the suction side continues (cf. Figure IV.23b). Subsequently, a significant concentration of accumulated CCW vorticity is shed and there is a decrease in the CW vorticity (cf. Figure IV.23b), which result in an increase in circulation beginning at $t/\tau_{\text{conv}} = 0.21$ over a period of $0.15 \tau_{\text{conv}}$ and an overshoot of 32% relative to the final stationary level. When the

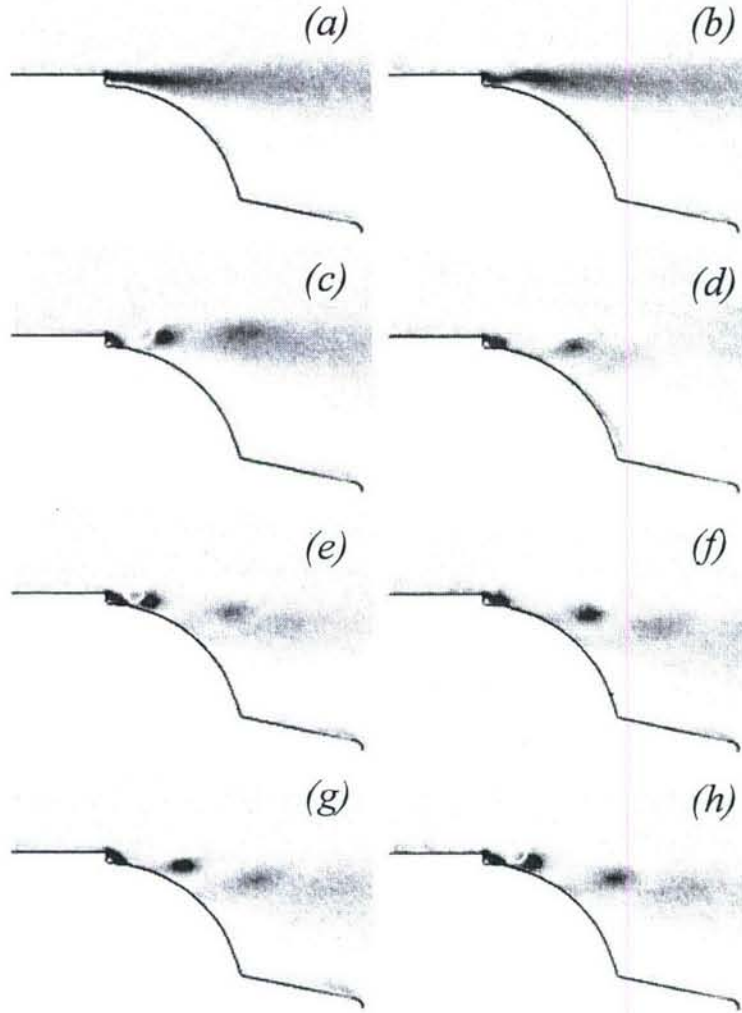


Figure IV.25. Vorticity fields following initiation of actuation at $t/\tau_{\text{conv}} = 0$: $t/\tau_{\text{conv}} = (a-h) 0, 0.03, 0.06, 0.12, 0.18, 0.30, 0.42, 0.54$. Clockwise vorticity is indicated in blue, counterclockwise vorticity in red.

actuation is switched from the *SS* to the *PS* actuators (Figure IV.24b), the drop in circulation and corresponding decrease in lift is preceded by an initial increase in circulation suggesting an initial increase in trapped CW vorticity (a similar rise was observed by Amitay and Glezer 2006 during the termination of actuation for an airfoil at post-stall angle of attack). The initial increase is followed by a large transitory reduction in circulation as a result of accumulation of CCW vorticity by the *PS* actuator before the circulation settles to a lower stationary level. The circulation undershoot and overshoot and some oscillations that follow the primary transition in circulation may be coupled to a near wake instability having a characteristic period of $0.15\tau_{\text{conv}}$

(cf. DeSalvo and Glezer 2006, 2007). The overall change in the level of the scaled circulation ($\Delta\Gamma^* = 0.082$, i.e. $0.19C_{L0}$) between the two stable actuation conditions corresponds approximately to the change in C_L (cf. Figure IV.21), assuming that $\Gamma^* = C_L$ for nominally *steady* flow (though Γ^* does not correspond with the variation of *unsteady* lift during the transient period).

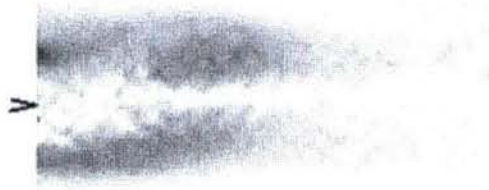


Figure IV.26. Wake vorticity map at $t/\tau_{\text{conv}} = 0.12$ following onset of suction surface actuation. Colors as in Figure IV.25. Mark at left denotes trailing edge of airfoil.

The effects of the initiation of actuation on the flow field in the immediate vicinity of the suction actuator are shown in the maps of vorticity concentrations (Figure IV.25) that are measured phase-locked to the actuation waveform (the imaged field measures 32 x 32 mm, and the magnification is 33 $\mu\text{m}/\text{pixel}$). It should be noted that the cross stream height of the turbulent boundary layer upstream of the actuator orifice (located at $x/c = 0.95$) extends well above the top end of the image and therefore the CW (blue) vorticity layer above the surface upstream of the actuator extends through the top edge of the frame. Prior to the onset of actuation (at $t/\tau_{\text{conv}} = 0$), there is a layer of CW vorticity that is detached from the wall downstream of the actuator orifice (Figure IV.25a) and is accompanied by a recirculating flow (trapped vorticity) domain that produces a thin layer of CCW (red) vorticity along the wall. At $t/\tau_{\text{conv}} = 0.03$ (Figure IV.25b), the activation of the actuator disrupts the separated layer and leads to the shedding of a

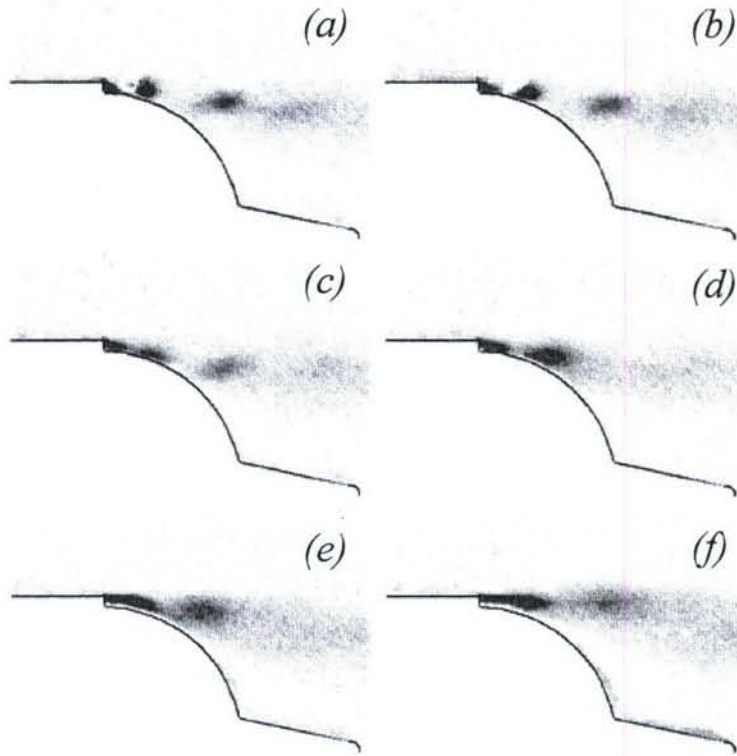


Figure IV.27. Vorticity fields following termination of actuation at $t/\tau_{\text{conv}} = 0$: $t/\tau_{\text{conv}} =$ (a-f) 0, 0.03, 0.06, 0.09, 0.15, 0.21. Colors as in Figure IV.25.

concentration of CW vorticity as shown in the vorticity map of the near wake (at $t/\tau_{\text{conv}} = 0.12$) in Figure IV.26, which consequently results in a momentary reduction in lift (cf. Figure IV.24a). A counterrotating vortex pair forms near the actuator orifice, as seen at $t/\tau_{\text{conv}} = 0.06$ (Figure IV.25c) and begins to propagate downstream while farther downstream ($\Delta x \approx 0.025c$ downstream of the actuator) the remnants of the separated vorticity layer (that was present at $t/\tau_{\text{conv}} = 0$) are shed into the wake. A portion of the CW vorticity produced by the actuator remains attached to the wall ($t/\tau_{\text{conv}} = 0.12$; Figure IV.25d), reducing the size of the vorticity domain downstream of the actuator and leading to an overall rise in (time-averaged) vorticity concentrations near the actuator. The CCW vortex induced by the actuator has diminished in strength and advected above the considerably stronger CW vortex, which is relatively close to the wall. Continued operation of the actuator causes additional vortex pairs to form at the actuator and persist briefly before they are advected downstream. As a result of the actuation, the flow near the trailing edge is turned toward the airfoil surface while CW vorticity concentrations are shed into the wake (Figures IV.25e-h).

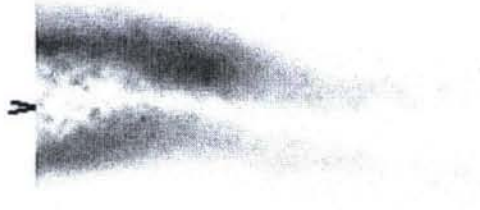


Figure IV.28. Wake vorticity map at $t/\tau_{\text{conv}} = 0.27$ following termination of suction surface actuation. Colors as in Figure IV.25. Mark at left denotes trailing edge of airfoil.

Similarly, Figure IV.27 shows the evolution of the vorticity field following the *termination* of actuation on the suction surface (Figure IV.27a). The separated vorticity layer downstream of the actuator begins to reform at $t/\tau_{\text{conv}} = 0.03$ (Figure IV.27b) and becomes more apparent by $t/\tau_{\text{conv}} = 0.06$ (Figure IV.27c); however, it has not yet stabilized, as indicated by the interruption downstream of the actuator orifice. During this time the separation point (located near the point where the sense of the wall vorticity changes) remains in the same approximate location. By $t/\tau_{\text{conv}} = 0.09$ (Figure IV.27d) the concentration of CW vorticity downstream of the interruption has started to detach from the wall, while the separation point along the wall moves upstream. The vorticity concentration propagates downstream, becomes detached from the wall by $t/\tau_{\text{conv}} = 0.15$ (Figure IV.27e), and continues to be advected into the wake at $t/\tau_{\text{conv}} = 0.21$ (Figure IV.27f) while the vorticity layer stabilizes near the actuator. The location of the detached vortex within the near wake is shown for $t/\tau_{\text{conv}} = 0.27$ in Figure IV.28. After a period of τ_{conv} (cf. Figure IV.24), the flow settles into the configuration shown in Figure IV.25a.

IV.4.2 Aerodynamic Control using Modulated Actuation

Alternate, pulse modulated activation of the hybrid actuator is used to achieve proportional *bi-directional* control of the pitching moment relative to some desirable trim condition. To this end, the transitory effects discussed in §IV.4.1 are exploited in order to maximize the control authority of the actuator over a broad range of angles of attack. The earlier work of DeSalvo and Glezer (2005) demonstrated that the airfoil's aerodynamic characteristics can be continuously varied simply by adjusting the actuator momentum coefficient C_μ through the amplitude of the actuation waveform. However, this variation is nonlinear and is clearly dependent on the characteristics of the actuator (e.g. at very low actuation amplitudes the jet formation may be unstable). For these reasons it is useful to operate the actuator using pulse width modulation and vary its duty cycle for a given C_μ . As shown by DeSalvo and Glezer (2006), by exploiting transitory effects, pulse modulated actuation can yield aerodynamic performance that is equal to or greater than what is achieved with continuous (unmodulated) actuation with lower actuation power. The effects of actuation increase with increasing duty cycle, and seem to peak when the modulation frequency is commensurate with the unstable frequencies of the near wake.

These considerations suggest that alternate, pulse modulated operation of two actuators mounted on opposite surfaces near the trailing edge can yield desired, controllable variation in the aerodynamic performance. In the present implementation, complementary pulse-modulated actuation waveforms are applied to the *SS* and *PS* actuators in order to vary C_M between the pitching moments that are effected by continuous operation of each of actuators. As shown in connection with Figure IV.20, the achievable pitching moments are almost invariant across a broad range of angles of attack when the baseline flow is fully attached. Therefore, the *PS* and *SS* actuators are operated at actuation levels that correspond to the minimum and maximum levels of C_M and are pulse modulated *complementary* to each other at variable duty cycle such that only one actuator is active at any one time to produce a continuous variation in the magnitude of C_M . Based on transitory response of I^* in Figure IV.24, the modulation (or repetition) frequency of the (pulse) modulating waveform is selected so that the *PS* actuator is operated for $0.42\tau_{\text{conv}}$ of each modulation period while the *SS* actuator is operating the remainder of the time.

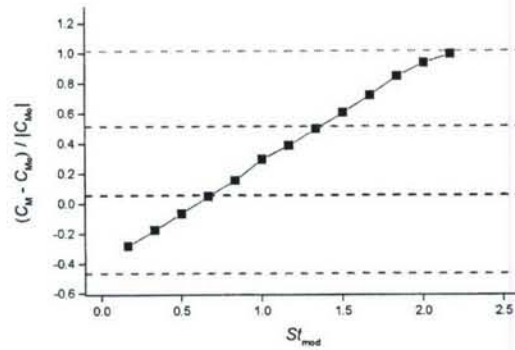


Figure IV.29. Variation of $(\Delta C_M / |C_{M0}|)$ operating pressure surface actuator in pulses of duration 0.42τ and suction surface actuator the remainder of the time (■). Unmodulated actuation: (—) Unactuated, (—), Pressure surface actuation only, (—) Suction surface actuation only, (—) Both actuators operating.

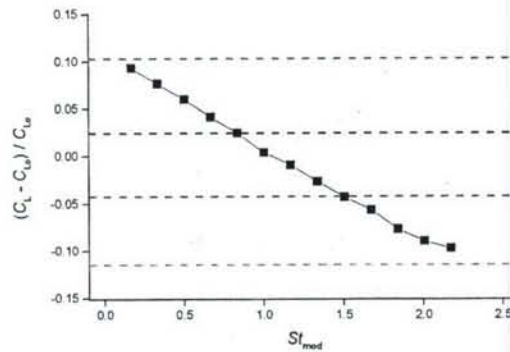


Figure IV.30. Variation of $(\Delta C_L / C_{L0})$; modulation scheme and symbols as in Figure IV.29.

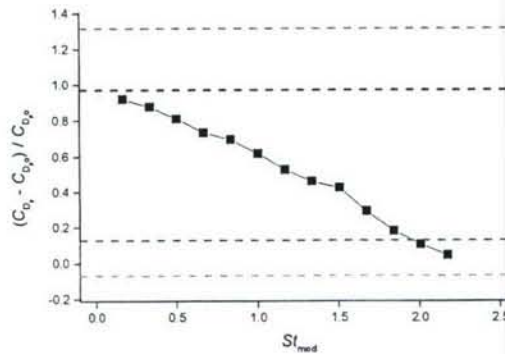


Figure IV.31. Variation of $(\Delta C_{Dp} / C_{Dp0})$; modulation scheme and symbols as in Figure IV.29.

V. CONCLUSIONS

The aerodynamic performance of a swept wing is controlled by leveraging the presence of localized trapped vorticity concentrations that are engendered by one or more hybrid actuators on the pressure and suction surfaces near the leading and trailing edges of the airfoil when the baseline flow is fully attached. The vorticity concentrations are manipulated in such a manner that the pressure distribution around the airfoil is altered, yielding significant reduction in drag in most configurations, along with substantial bi-directional changes in the pitching moment. Actuation is effected using hybrid actuators consisting of a miniature obstruction having a characteristic scale of $O(0.01c)$ which forms a domain of trapped vorticity and an integral synthetic jet having momentum coefficient $C_\mu = O(10^{-3})$ which is used to regulate the vorticity concentrations that form downstream of the obstruction.

When a single hybrid actuator is placed just upstream of the trailing edge on the pressure side, there is a small increase in lift which is accompanied by increased pressure drag and therefore a reduction in the lift to pressure drag ratio (L/D_p). Continuous high-frequency actuation results in the formation of a localized low-pressure domain between the downstream edge of the actuator and the trailing edge of the airfoil, altering the flow in the region and reversing some of the changes in the pressure distribution that are induced by the inactive actuator. The pressure at the trailing edge increases and the wake of the airfoil is turned upward. The actuation results in a substantial increase in L/D_p compared to both the baseline (smooth) airfoil and the inactive actuator configuration. The maximum lift to drag ratio $L/D_p = 34.1$ is obtained at $\alpha = 6^\circ$ which is an increase of 40% over the inactive actuator airfoil, but more significantly an increase of 20% over the smooth airfoil.

High-resolution particle image velocimetry (PIV) is used to obtain detailed information about the flow field in the vicinity of the actuator to determine the effects of the actuation on the structure of the near wake and the flux of vorticity into the wake. When actuation is initiated, a disruption is created in the separated vorticity layer at the actuator orifice that causes a large vorticity concentration to be shed into the wake. The actuation generates pairs of vorticity concentrations of alternating (opposite) sense which are subsequently advected downstream; the concentration of opposite sense to the boundary layer diminishes rapidly, while the other concentration remains attached to the wall before being shed into the wake downstream of the actuator. This causes the

separation point along the wall to move downstream, reducing the extent of the recirculating flow domain near the actuator thus altering the rear stagnation point and thereby the aerodynamic characteristics of the entire airfoil. Deactivation of the actuator causes a vorticity cluster to be shed into the wake before a stable detached layer of vorticity is reestablished near the actuator orifice.

Phase-locked PIV studies have been conducted to determine the time varying characteristics of the wake under pulse modulated actuation. The vorticity flux across the near wake ($\sim 0.05c$ downstream of the trailing edge) is computed and integrated to obtain the time rate of change of circulation, from which the variation of circulation over time around the entire airfoil is computed. Initiation of actuation leads to changes in the circulation on the timescale of $1-2\tau_{\text{conv}}$ along with more rapid variations on the timescale of $\sim 0.15\tau_{\text{conv}}$, corresponding to a reduced modulation frequency of $St_{\text{mod}} = 6.7$ which corresponds to the characteristic frequency of the unstable wake. Actuation also leads to a reduction in the velocity deficit in the wake along with a shift toward the trailing edge, both of which develop on the same time scales as the changes in circulation.

Placement of a hybrid actuator near the leading edge on the pressure surface leads to a significant (nominally 50%) reduction in pressure drag with minimal lift penalty (nominally 9%). The presence of the actuator results in the formation of a domain of trapped vorticity near the actuator orifice which leads to a local acceleration of the flow immediately upstream of the actuator. It has been shown in these studies that by controlling the streamwise extent of the induced concentrations of trapped vorticity and therefore the magnitude and streamwise extent of the local suction peak near the actuator orifice it is possible to continuously reduce the pressure drag of the airfoil and concomitantly increase the lift to drag ratio. For this configuration of the airfoil and hybrid actuator, the skin friction drag C_{Df} is estimated from integration of the wall friction coefficient around the airfoil that is obtained from detailed PIV measurements of streamwise velocity within the surface boundary layer. For the baseline configuration (where the boundary layer is laminar along much of the pressure surface), $C_{\text{Df}} = 0.0058$. In the presence of the actuator $C_{\text{Df}} = 0.0081$ when the actuator is inactive and 0.0076 when the jet is activated. The total drag coefficients for the airfoil for the three configurations tested are $C_{\text{D}} = 0.0170$ (baseline), 0.0192 (inactive hybrid actuator) and 0.0121 (jet actuation). *These results show that for $\alpha = 4^\circ$*

and $Re_c = 6.7 \cdot 10^5$, the actuation leads to a 29% reduction of the total drag relative to the baseline airfoil and therefore to an increase of 27% in L/D from 28.3 to 35.8.

It is remarkable that the *simultaneous* formation of trapped vorticity concentrations can lead to a superposition of their individual effects. For example, the formation of such concentrations near the leading and trailing edges of the airfoil leads to a significant increase in lift in the absence of actuation. Actuation near the leading edge only results in reduction of the pressure drag of up to 42% relative to the unactuated airfoil at $\alpha = 4^\circ$ with virtually no change in lift or moment (about $c/4$). Actuation near the trailing edge leads to an independent additional reduction in pressure drag (58% relative to the unactuated airfoil with a small penalty of about 5% in lift) and also to alteration of the pitching moment. Simultaneous operation of both actuators reduces the pressure drag at $\alpha = 4^\circ$ to $\underline{C}_{Dp} = 0.0003$ from $C_{Dp} = 0.0085$ for the baseline airfoil.

The formation of independently controlled trapped vorticity domains on the pressure and suction surfaces of the airfoil near the trailing edge is used to effect control of the airfoil pitching moment in the absence of moving control surfaces. Continuous operation of either actuator leads to substantial changes in the pitching moment over a broad range of angles of attack that are bi-directional relative to the moment of the unactuated airfoil (the pressure and suction surface actuators induce relative pitch-up and -down moments, respectively). The present measurements show that the levels of C_M effected by each actuator at maximum actuation power are reasonably independent of α over the range $-2^\circ < \alpha < 9^\circ$ and that the nominal range of moment values span $1.4C_{M0}$ (where C_{M0} is the moment of the baseline airfoil). The magnitude of the induced moment (and other aerodynamic characteristics) depends on the location of the actuator and placement of the suction surface actuator at $0.90c$ expands the overall range of moment variation to $1.6C_{M0}$ (with a somewhat larger drag penalty). Actuation can also be used to adjust C_L across a range of $\Delta C_L \approx 0.1$. While operation of the pressure surface actuator leads to pressure drag levels that are comparable to the smooth airfoil (and a slight reduction in lift), operation of the suction side actuator results in a small increase in pressure drag (17% at $\alpha = 6^\circ$ compared to the smooth airfoil) and a slight increase in lift.

The actuation effectiveness can be substantially increased by exploiting transitory effects that are associated with the onset and termination of the actuation input thereby leading to improved performance at reduced input power. This is investigated by comparing the effect of continuous

and amplitude (pulse) modulated actuation having the same input power. Power levels are adjusted by varying the amplitude of the continuous waveform and the frequency and duty cycle of the modulating waveform. It is shown that *the aerodynamic performance of the present airfoil can be continuously varied without the use of control surfaces* between the levels of a high-lift airfoil (but with lower L/D relative to the baseline) and an airfoil that has improved L/D (relative to the baseline). Performance improvements can be realized at lower actuation power using pulse width modulation of the actuation waveform. In particular, operating the trailing edge actuator on the pressure surface at a reduced modulation frequency that is coupled to the instability of the near wake ($St_{mod} = 6.7$) and a duty cycle of 0.25 reduces the drag to the same level as with continuous actuation at full power, with only a minimal lift penalty in both cases. There is even greater drag reduction when the actuator is operated at $St_{mod} = 6.7$ and duty cycle 0.9.

Continuous variation of the airfoil aerodynamic characteristics that is achievable through pulse modulated actuation is exploited in the dual trailing edge actuator configuration to achieve proportional *bi-directional* control of the pitching moment relative to some desirable trim condition where transitory effects are exploited to maximize the control authority over a broad range of angles of attack. Because the variation in the aerodynamic characteristics depends nonlinearly on actuation voltage it is useful to operate the actuator using pulse width modulation and vary the duty cycle and modulation frequency for a given C_μ to achieve a desired, controllable variation in the aerodynamic performance. A nearly linear variation in pitching moment with modulation frequency can be achieved over a nominal range of $1.28C_{M0}$ (at $\alpha = 4^\circ$). The application of pulse width modulation also alters the corresponding changes in pressure drag. When the pressure surface actuator is mostly operational the pressure drag is comparable to the pressure drag of the smooth airfoil, and when the suction surface actuator is mostly operational, the pressure drag is 30% *less* than with continuous actuation of the suction surface actuator. As a result, C_M can be varied over nearly the same range of levels as with continuous actuation but with lower drag penalty.

- DeSalvo, M., Amitay, M., and Glezer, A., "Modification of the Aerodynamic Performance of Airfoils at Low Angles of Attack: Trailing Edge Trapped Vortices," AIAA Paper 2002-3165.
- DeSalvo, M. and Glezer, A., "Aerodynamic Performance Modification at Low Angles of Attack by Trailing Edge Vortices," AIAA Paper 2004-2118.
- DeSalvo, M. and Glezer, A., "Airfoil Aerodynamic Performance Modification using Hybrid Surface Actuators," AIAA Paper 2005-0872.
- DeSalvo, M. and Glezer, A., "Aerodynamic Control at Low Angles of Attack using Trapped Vorticity Concentrations," AIAA Paper 2006-0100.
- DeSalvo, M. and Glezer, A., "Control of Airfoil Aerodynamic Performance using Distributed Trapped Vorticity," AIAA Paper 2007-0708.
- Erk, P. P., "Separation Control on a Post-Stall Airfoil Using Acoustically Generated Perturbations," Ph.D. Dissertation, Technische Universitat Berlin, Germany, 1997.
- Giguère, P., Lemay, J., and Dumas, G., "Gurney Flap Effects and Scaling for Low-Speed Airfoils", AIAA Paper 95-1881.
- Glezer, A. and Amitay, M. "Synthetic Jets," *Ann. Rev. Fluid Mechanics*, 24, 2002.
- Glezer, A., Amitay, M., and Honohan, A., "Aspects of Low- and High-Frequency Actuation for Aerodynamic Flow Control," *AIAA Journal* 43(7), pp. 1501-1511, 2005.
- Hsiao, F.-B., Liu, C.-F., and Shyu, J.-Y., "Control of wall-separated flow by internal acoustic excitation," *AIAA Journal* 28(8), pp. 1440-1446, 1990.
- Hurley, D. G., "The Use of Boundary Layer Control to Establish Free Stream Line Flows," *Adv. Aero Sci.* 2, 662, 1959.
- Jang, C., Ross, J., and Cummings, R., "Computational Evaluation of an Airfoil with a Gurney Flap," AIAA Paper 92-2708.
- Jeffrey, D., Zhang, X., and Hurst, D., "Aerodynamics of Gurney Flaps on a Single-Element High-Lift Wing," *Journal of Aircraft* 37(2), pp. 295-301, 2000.
- Liebeck, R.H., "Design of Subsonic Airfoils for High Lift," *Journal of Aircraft* 15(9), pp. 547-561, 1978.
- Mandl, P., "Effect of Standing Vortex on Flow about suction aerofoils with Split Flaps," *Nat. Res. Council of Canada, Aero. Rep. No. 234*, 1959.

- Myose, R., Papadakis, M., and Heron, I., "Gurney Flap Experiments on Airfoils, Wings, and Reflection Plane Model," *Journal of Aircraft* 35(2), pp. 206-211, 1998.
- Perkins, C. D. and Hazen, D., "Some recent advances in Boundary Layer and Circulation Control," Fourth Anglo-American Aeronautical Conference, 1953.
- Richter, K. and Rosemann, H., "Experimental investigation of trailing-edge devices at transonic speeds," *The Aeronautical Journal* 106(1058), pp. 185-193, 2002.
- Seifert, A., Bachar, T., Koss, D., Shepshelovich, M. and Wygnanski, I., "Oscillatory blowing: A tool to delay boundary-layer separation," *AIAA Journal* 31(11), pp. 2052-2060, 1993.
- Seifert, A., Darabi, A., and Wygnanski, I., "Delay of Airfoil Stall by Periodic Excitation," *Journal of Aircraft* 33(4), pp. 691-698, 1996.
- Smith, B. L. and Glezer, A. "The Formation and Evolution of Synthetic Jets," *Physics of Fluids* 10(9), p. 2281-2297, 1998.
- Smith, B. L. and Glezer, A., "Jet vectoring using synthetic jets," *J. Fluid Mech.*, 458, pp. 1-34, 2002.
- Smith, D. R., Amitay, M., Kibens, V., Parekh, D. E. and Glezer, A., "Modification of Lifting Body Aerodynamics using Synthetic Jet Actuators," AIAA Paper 98-0209.
- Wu, J.-Z., Lu, X.-Y., Denny, A. G., Fan, M., and Wu, J.-M., "Post Stall Flow Control on an Airfoil by Local Unsteady Forcing," *J. Fluid Mech.*, 371, pp. 21-58, 1998.
- Wu, J.-Z., Vakili, A. D., and Wu, J.-M., "Review of the Physics of Enhancing Vortex Lift by Unsteady Excitation," *Prog. Aerospace Sci.*, 78, pp. 73-131, 1991.
- Wygnanski, I., "The Variables Affecting the Control of Separation by Periodic Excitation," AIAA Paper 2004-2505.